

AD-A252 420



2

OFFICE OF NAVAL RESEARCH

Research Contract: N00014-90-J-1178

R&T Code: 413r008---01

Principal Investigator: **R. Stanley Williams**

Organization: **Regents of the University of California**

TECHNICAL REPORT No. 16

**CORRELATION FROM RANDOMNESS: QUANTITATIVE ANALYSIS OF SPUTTERED
GRAPHITE SURFACES USING THE SCANNING TUNNELING MICROSCOPE**

by

E.A. Eklund, E.J. Snyder and R.S. Williams

Prepared for publication in

Surface Science



University of California, Los Angeles

Department of Chemistry & Biochemistry and Solid State Sciences Center

Los Angeles, CA 90024-1569

Reproduction in whole, or in part, is permitted for
any purpose of the United States Government

This document has been approved for public release and sale; its distribution is unlimited



REPORT DOCUMENTATION PAGE

Form Approved
OMB No 0704-0188

Public reporting burden for this collection of information is estimated to average 1 hour per response, including the time for reviewing instructions, searching existing data sources, gathering and maintaining the data needed, and completing and reviewing the collection of information. Send comments regarding this burden estimate or any other aspect of this collection of information, including suggestions for reducing this burden, to Washington Headquarters Services, Directorate for Information Operations and Reports, 1215 Jefferson Davis Highway, Suite 1204, Arlington, VA 22202-4302, and to the Office of Management and Budget, Paperwork Reduction Project (0704-0188), Washington, DC 20503.

1. AGENCY USE ONLY (Leave blank)		2. REPORT DATE 10 March 1992		3. REPORT TYPE AND DATES COVERED Technical 6/1/91-5/31/92	
4. TITLE AND SUBTITLE CORRELATION FROM RANDOMNESS: QUANTITATIVE ANALYSIS OF SPUTTERED GRAPHITE SURFACES USING THE SCANNING TUNNELING MICROSCOPE				5. FUNDING NUMBERS N00014-90-J-1178	
6. AUTHOR(S) E.A. Eklund, E.J. Snyder, R.S. Williams					
7. PERFORMING ORGANIZATION NAME(S) AND ADDRESS(ES) Regents of the University of California University of California 405 Hilgard Ave. Los Angeles, CA 90024				8. PERFORMING ORGANIZATION REPORT NUMBER Technical Report #16	
9. SPONSORING MONITORING AGENCY NAME(S) AND ADDRESS(ES) Office of Naval Research Chemistry Program 800 N. Quincy Street Arlington, VA 22217-5000				10. SPONSORING / MONITORING AGENCY REPORT NUMBER	
11. SUPPLEMENTARY NOTES Preparation for publication in "Surface Science"					
12a. DISTRIBUTION AVAILABILITY STATEMENT Approved for public release. Distribution unlimited.				12b. DISTRIBUTION CODE	
13. ABSTRACT (Maximum 200 words) The Scanning Tunneling Microscope (STM) was used to quantitatively examine the surface morphology of highly oriented pyrolytic graphite (HOPG) surfaces bombarded with 5 keV Ar ⁺ ions. Constant current topographs clearly showed that the morphology of the resulting nonequilibrium surfaces depended sensitively on the ion flux, the ion fluence and the sample temperature. For low and intermediate ion fluence, an increase in surface roughness with increasing ion flux was observed. For constant ion flux, the surfaces developed structures with heights proportional to the ion fluence and separations characterized by a correlation length that diverged with increasing fluence. Increasing the sample temperature during bombardment produced smoother surfaces as a result of enhanced surface diffusion. The autocovariance function G(L) and the height correlation function $h(q)^2$ in reciprocal space were calculated directly from the STM topographs. The latter was then compared with a linear response theory for the formation of rough surfaces under nonequilibrium conditions and a scaling analysis. The fluence dependence of the surface roughening of graphite could not be explained by shot noise alone in a linear theory, whereas surface diffusion and redeposition of sputtered material satisfactorily accounted for the correlation observed in the bombardment-induced features.					
14. SUBJECT TERMS				15. NUMBER OF PAGES 62 pages	
				16. PRICE CODE	
17. SECURITY CLASSIFICATION OF REPORT Unclassified	18. SECURITY CLASSIFICATION OF THIS PAGE Unclassified	19. SECURITY CLASSIFICATION OF ABSTRACT Unclassified	20. LIMITATION OF ABSTRACT UL		

13-157-
D-1-14-11

**Correlation From Randomness: Quantitative Analysis of Sputtered Graphite
Surfaces Using the Scanning Tunneling Microscope**

Elliott A. Eklund^{*1,3}, Eric J. Snyder^{2,3} and R. Stanley Williams^{2,3}

¹Department of Physics

²Department of Chemistry and Biochemistry

³Solid State Science Center

University of California Los Angeles, CA 90024

Abstract: The Scanning Tunneling Microscope (STM) was used to quantitatively examine the surface morphology of highly oriented pyrolytic graphite (HOPG) surfaces bombarded with 5 keV Ar⁺ ions. Constant current topographs clearly showed that the morphology of the resulting nonequilibrium surfaces depended sensitively on the ion flux, the ion fluence and the sample temperature. For low and intermediate ion fluence, an increase in surface roughness with increasing ion flux was observed. For constant ion flux, the surfaces developed structures with heights proportional to the ion fluence and separations characterized by a correlation length that diverged with increasing fluence. Increasing the sample temperature during bombardment produced smoother surfaces as a result of enhanced surface diffusion. The autocovariance function $G(L)$ and the height correlation function $\langle |h(q)|^2 \rangle$ in reciprocal space were calculated directly from the STM topographs. The latter was then compared with a linear response theory for the formation of rough surfaces under nonequilibrium conditions and a scaling analysis. The fluence dependence of the surface roughening of graphite could not be explained by shot noise alone in a linear theory, whereas surface diffusion and redeposition of sputtered material satisfactorily accounted for the correlation observed in the bombardment-induced features.

I. Introduction

One of the fundamental challenges in materials science is to understand the effects of particle radiation on the nature of solid surfaces.¹⁻³ For example, the properties of sputter deposited thin films depend sensitively on the surface topology, which is determined by the sputter-growth process.⁴ A similar situation exists for ion-beam sputter etching, a widely used technique in surface science and microelectronics, which also produces nonequilibrium surfaces with topography that depends on the sputtering conditions.⁵

Erosion of surfaces by sputtering is important in a great variety of disciplines. In surface science experiments, clean surfaces are usually prepared by repeated cycles of sputtering with noble gas ions and annealing at elevated temperatures.⁶ In depth-profiling analyses, sputter etching is used to strip away successive layers of the sample, exposing sub-surface material for compositional determination.² With this technique, control of the surface roughness is important because the bombardment induced topography determines the depth resolution of the compositional analysis.^{7,8} Focused ion beam micromachining has been used in the electronics industry for the repair of X-ray lithography masks and the fabrication of device microstructures.⁹ In some cases, sputtering is an unwanted but important side effect of the environment, as in the erosion of the inner walls of fusion plasma containment vessels or the outer skins of space vehicles as they pass through the atmosphere. In fact, fusion plasma chambers commonly have a graphite interior lining¹⁰ and carbon composites are highly desirable materials for space vehicles because of their strength and light weight.¹¹ The experiments presented in this study are particularly relevant to the understanding of the sputtering of graphite and carbon composites, since ion



Dist		Avail and/or Special	
A-1			

<input checked="" type="checkbox"/>
<input type="checkbox"/>
<input type="checkbox"/>

bombardment should produce similar amorphous surfaces on both types of materials after a short time.

In general, surfaces exposed to high levels of particle radiation develop characteristic morphologies. On the macroscopic level (i.e., length scales larger than one micron), the effects of particle radiation are well understood. Ion bombardment erodes edges, corners and peaks preferentially because these prominent features are exposed to a larger incident flux. This radiation erosion is further enhanced by surface diffusion and evaporation/recondensation. In the continuum description of this process, one either assumes that the local erosion rates are proportional to the local incoming flux, or one uses the so-called "Huygens Construction",^{12,13} in which successive profiles of the eroding surface are treated as a propagating kinetic wave. In this latter method, one calculates the surface profile produced after a time Δt by constructing spherical erosion zones, which have radii proportional to the ion flux, the local sputtering yield and the time step Δt , at each point on the starting surface profile. The new surface profile is then given at each point by the envelope of these spherical erosion volumes. Numerical simulations of the macroscopic evolution of sputtered surfaces have produced results that compare favorably with experiments.^{14,15}

At the sub-micron level, our understanding is much less complete.¹⁶ Electron-microscope studies of sputtered surfaces indicate that particle radiation will *roughen* the surface rather than smooth it, and prominent cone-like features have been reported.¹⁷⁻¹⁹ The stochasticity of the bombardment process can be included in theoretical models by adding a term describing shot noise, the variation of the incident flux around some mean value. Both analytical studies and Monte Carlo simulations^{20,21} of the effect of shot noise on continuum theories of growth by sputter deposition indicate that such nonequilibrium surfaces evolve roughness. The features produced are characterized by a

correlation length $\xi(t)$ which diverges with deposition time t . Similar results are expected for the case of sputter etching, but until now there has been little experimental confirmation of this description.

Our use of the Scanning Tunneling Microscope (STM)^{22,23} to examine the surface topography of graphite after sputter etching offered many unique opportunities for the study of nonequilibrium surfaces. Unlike the scanning electron microscope (SEM), which has been the primary analysis tool for imaging the topography of sputtered materials, the STM can *quantitatively* measure the height profile $h(r)$ of the surface over a wide range of lateral and vertical length scales, with a lateral resolution of better than 10 Å and a vertical resolution of a fraction of an Ångström.^{22,23} This allowed us to calculate from the topographs the auto-covariance function,²⁴ defined as:

$$G(|\mathbf{r}_2 - \mathbf{r}_1|) = \langle h(\mathbf{r}_2)h(\mathbf{r}_1) \rangle - \langle h(\mathbf{r}) \rangle^2, \quad (1)$$

where $h(\mathbf{r}_i)$ is the height of the surface at position \mathbf{r}_i and $L = |\mathbf{r}_2 - \mathbf{r}_1|$ is a separation length on the surface, and the height correlation function, defined as:

$$\langle |h(\mathbf{q})|^2 \rangle = \int \frac{d^2\mathbf{r}}{(2\pi)^2} e^{i\mathbf{q} \cdot \mathbf{r}} \langle (h(0) - h(\mathbf{r}))^2 \rangle_t / \text{Area}, \quad (2)$$

with $\langle \dots \rangle_t$ indicating a sample average after t seconds of exposure. The calculation of the auto-covariance function G provided a quantitative determination in real space of the base to peak height variation and the short range lateral correlation of the surface features. Calculation of the height correlation function $\langle |h(\mathbf{q})|^2 \rangle$ allowed us to determine the reciprocal space scaling behavior of the surfaces as a function of the wavenumber q and to make

comparisons of our experimental data to existing theories of surface morphology created by sputter erosion. In other surface roughening problems, *e.g.*, thermal roughening, this correlation function was found to be a good measure of the surface geometry.²⁵ Because of loss of phase information in the height correlation function, however, it is less sensitive to uncorrelated -- but prominent - surface features, which are much more easily visible in the real space STM topographs.

The STM has been used by other researchers to study rough surfaces produced by fracture and deposition by sputtering and evaporation.²⁶⁻²⁸ These studies have addressed some of the special problems associated with the scanning of rough surfaces with a tunneling microscope, in particular, that the STM topographs can depend on the shape and sharpness of the tip and on the roughness of the surfaces. Asymmetric tips will produce artificial anisotropy in the images while blunt tips will fail to reproduce small, closely spaced features.²⁹ Surfaces with very sharp protrusions will yield images of the sides of the tunneling tip instead of the surface features.³⁰ We have been particularly careful to check that tip related artifacts have not contributed seriously to the topographs in this study. Other factors that must be considered include the maximum size of the tunneling microscope scans and the density of the data points in a topograph.

A major difference between this and previous studies of sputter-induced topography was that the freshly cleaved graphite surfaces were atomically flat over tens of thousands of square Ångströms³¹ before bombardment. This allowed us to investigate the *initial* stages of sputter induced morphology from flat surfaces starting with low ion fluences (10^{16} ions/cm²) and to characterize the *evolution* of the surface profile as a function of time. The real space topographs, the auto-covariance functions and the height correlation functions provided complementary information that allowed us to investigate the dependence of the

surface morphology of sputtered graphite on several of the most commonly varied sputtering parameters. The surfaces were sensitive to variations in ion flux, ion fluence and sample temperature. In particular, for the *lowest* ion fluences, the base to peak height variations of the sputtered surfaces increased with increasing ion flux. For all fluxes used, the correlation length and the vertical size of the surface features increased as the fluence was increased. Moreover, the size of the features scaled approximately linearly with the fluence, which is surprising for an essentially stochastic process. Sputtering at elevated sample temperatures produced surfaces that were smoothed by enhanced surface diffusion.

II. Experimental Procedure

The STM used in these experiments was of the flip stage design introduced by Demuth et al.³² Our instrument was designed to operate at atmospheric pressure and a variety of precautions were taken to make the microscope insensitive to mechanical, electrical, and thermal disturbances in the laboratory. The mechanical isolation of the instrument was accomplished in two stages; the STM assembly was placed on a platform hung from rubber cords to isolate it from low frequency room vibrations (1 - 10 Hz) and the microscope stage itself rested on another isolation stage of steel plates separated by viton rubber³³ which served to damp out higher frequencies. Isolation of the STM electronics was accomplished by careful shielding of sensitive components and by making all ground connections to a single, high quality ground point.³⁴ For the experiments in this study, the total electronic and mechanical noise was less than 2% of the tunneling signal, which meant that the rough surface features seen in the STM topographs of sputtered graphite had no significant system noise contributions. Thermal drift is a serious problem in many tunneling microscopes operating at atmospheric pressure and can cause distortion in STM images. The constant current imaging mode with its slower scanning speeds was needed for the

roughened graphite samples and required approximately 2 minutes to acquire a full topograph, making the images susceptible to drift. The thermally induced drift rates for our instrument were low, however, approximately 1 Å/min for the X and Y scanning axes, and had a negligible effect on the images. A final level of acoustical, electrical and thermal isolation was provided by an enclosure lined with acoustically absorbant foam and a grounded copper mesh which surrounded the STM during scanning.

The 3 axis piezo-electric drive²² that positioned the tunneling tip was carefully calibrated before any distance measurements were made on samples with disordered topography. Two independent methods were used to calibrate the STM. The atomically resolved features³⁵ seen on graphite at high magnification were used to calibrate the piezo drives for small displacements (image size of 25 Å x 25 Å). This calibration was supplemented with interferometric measurements³⁶ that required the piezo-electric elements to be scanned several thousand Ångstroms at a time, resulting in sensitivities for the X, Y and Z axes of 12.91 ± 0.33 , 12.28 ± 0.34 and 9.25 ± 0.29 Å/Volt, respectively. The tunneling tips were easily prepared by cutting Pt/Rh thermocouple wire, chosen because it does not form an insulating oxide layer in air, at an acute angle with ordinary wire cutters. It has been shown that mechanical cutting produces tips with many jagged protrusions, one of which acts as the actual tunneling tip.³⁷ This technique of tip preparation has been used successfully by other groups^{38,39} and routinely yielded atomic resolution in our imaging of clean, unbombarded graphite.

The surface chosen for this investigation was the (0001) face of highly oriented pyrolytic graphite (HOPG), which was easily cleaved with adhesive tape to produce large, atomically flat regions.²⁶ This surface was inert in air and easily imaged with the STM.³⁵ Graphite also has a rigid lattice, as seen by its

melting temperature of $\sim 3800^{\circ}\text{C}$. This indicates that surface diffusion effects were minimal and that topographical features produced by the bombardment were 'frozen in' and could be observed with the STM long after the sputtering had taken place. In general, surface diffusion is an important effect which smooths out surface features, so materials that can anneal at ambient temperatures are unsuitable for the experiments described here.

The constant current or topographic mode²² was used to collect the STM images, with a tunneling current of 0.5 nA and a sample to tip bias of -100 mV. Topographs collected at the largest possible scan size ($2400 \text{ \AA} \times 2400 \text{ \AA}$) showed large, atomically flat areas, while at higher magnifications (eg. $25 \text{ \AA} \times 25 \text{ \AA}$) the familiar atomic scale features of clean graphite were easily observed.³⁵

After stable images of clean graphite were obtained at both high and low magnifications, the samples were transferred to the sample treatment chamber of a KRATOS XSAM-800 surface analytical system. The graphite surfaces were then sputter etched at room temperature with a beam of 5 keV Ar^+ ions, rastered over a 9 mm^2 area on the sample and incident at an angle of 60° to the surface normal. The flux incident on the sample was determined by using an electrometer to measure the ion beam current. A small positive bias (45 volts) was applied to the sample to suppress secondary electron emission. The experimental parameters that were varied in this study were the flux J , the ion fluence $Q = Jt$, and the sample temperature T .

This paper highlights the results obtained from over 1,000 STM topographs collected from more than 15 bombarded graphite samples. The three ion fluxes reported here were $J_1 = 6.9 \times 10^{13}$, $J_2 = 3.5 \times 10^{14}$ and $J_3 = 6.9 \times 10^{14}$ ions/ $\text{cm}^2\text{-sec}$, corresponding to ion beam currents of approximately 1, 5 and 10 μA , respectively. The flux was varied by using different flow rates of Ar gas in the ion gun. By varying the time of exposure to the ion beam, the total fluences obtained were $Q_1 =$

10^{16} , $Q_2 = 10^{17}$ and $Q_3 = 10^{18}$ ions/cm². A sputtering yield of 1.5 carbon atoms ejected per incident argon ion was estimated by Monte Carlo simulations (TRIM code)⁴⁰ and, with 3.8×10^{15} carbon atoms/cm² at the graphite surface, the ion fluences given above corresponded to the removal of approximately 4, 40 and 400 monolayers of material, respectively, from the graphite surfaces. To investigate the effect of temperature (ie. enhanced surface diffusion) on sputter induced morphology, etching was also performed on samples heated to approximately 600K and 900K using the intermediate flux and fluence (J_2 and Q_2). The samples used for the variable temperature experiments were re-cleaved before each bombardment to return to the initial flat surface conditions. In addition, one graphite sample was annealed at 600 K after cleaving to release any surface stress and was allowed to cool before bombardment. The surfaces produced were similar to those sputtered without annealing before sputtering, indicating that the effects of cleaving on surface morphology created by ion bombardment were minimal.

The graphite samples were re-examined with the STM after etching using identical operating parameters and, if possible, the same tunneling tip used prior to sputtering. The results were reproducible from sample to sample and even with different tips, indicating that tip artifacts did not seriously affect the data. Topographs with serious artifacts were observed but were discarded from the data set. Fourteen different image sizes, ranging from 2400 Å x 2400 Å to 25 Å x 25 Å, were used to investigate each of the sputtered surfaces. Typically over 50 images of various sizes were collected at each location and several different locations were imaged on each sample. The topographical data for each image were digitally stored by the STM computer as arrays of 118 x 118 data points for subsequent viewing and calculations. In addition, the images were leveled by a least squares

fit of the data to a plane, thereby removing any effects of sample tilt but also possibly removing long wavelength features from the data.

The bombardment by 5 keV argon ions was expected to disrupt the graphite surfaces and possibly make them more prone than freshly cleaved samples to reaction with air. In fact, after 2 - 3 days of scanning sputtered surfaces with the STM, the images became noisy and some of the reproducibility was lost. These problems were avoided for the samples used in this study by minimizing the exposure of the surfaces to air during the time needed to acquire the topographs. At all other times, the samples were kept under vacuum in the etching chamber or were stored in a nitrogen filled glovebox, limiting the total air exposure for each surface to a maximum of a few hours.

III. Results and Qualitative Discussion of Topographs

The topographs presented in Figs. 1 - 4 show the behavior of the graphite surfaces at an image size of $2400 \text{ \AA} \times 2400 \text{ \AA}$ as the flux J , fluence Q and temperature T are varied. Each of the Figs. 1 - 3 shows a different ion fluence, and the effect of changing the ion flux for fixed fluence is shown within each of these figures. Fig. 4 illustrates the effect of sputtering at different temperatures. The reproducibility and scaling of surface features as the magnification is increased is demonstrated in Figs. 5 - 7.

The dependence of the morphology on the etching flux, for fixed fluence, is clearly seen in Figs. 1 - 3. For the lower fluences, Q_1 and Q_2 , Figs. 1 and 2 show that the surfaces became steadily rougher as the ion flux was increased. The three fluxes J_1 , J_2 and J_3 were in the ratio of $\sim 1:5:10$. The features in Figs. 1a, 1b and 1c have heights of ~ 4 , 20 and 40 \AA , respectively, while those in Figs. 2a, 2b and 2c have heights of ~ 10 , 30 and 60 \AA , roughly proportional to the ratio of the fluxes. Also apparent in Figs. 1 and 2 is the increasing amplitude of the short

wavelength roughness as the flux was increased. For the lowest flux, Figs. 1a and 2a show features separated by ~ 200 Å while Figs. 1c and 2c, showing surfaces sputtered with the highest flux, are dominated by features with separations < 100 Å. Features with both long and short length scales are seen for surfaces sputtered at the intermediate flux, shown in Figs. 1b and 2b. These trends are modified for the highest fluence Q_3 , shown in Fig. 3. The separation of surface features did not change significantly between the two lower fluxes, since Figs. 3a and 3b both show similar large structures separated by $\sim 1500 - 2000$ Å, but did decrease for the sample sputtered at the highest flux, which shows prominent features at smaller separations of ~ 800 Å in Fig. 3c.

The most striking effect seen in comparing Figs. 1 - 3 is the sensitivity of the surface morphology to the fluence Q , for all fluxes. In general, at the fluence of 10^{16} ions/cm² shown in Fig. 1, the surfaces all exhibited short range roughness of small amplitude, with features $4 - 40$ Å in height separated by distances of $50 - 200$ Å. Increasing Q to 10^{18} ions/cm² produced surfaces dominated by much larger features, $60 - 200$ Å high, with separation distances that approached the image size, as seen in Fig. 3. The transition between these extremes is shown clearly in Fig. 2 for surfaces sputtered at the intermediate fluence of 10^{17} ions/cm², where $4 - 10$ Å high features at small separations are seen along with hillocks that are 2 to 3 times higher at separations of several hundred Ångstroms.

Because of enhanced surface diffusion, it is expected that sputter etching of samples at elevated temperatures should yield surfaces that are less rough than those which are sputtered at ambient conditions. This prediction is confirmed in Figs. 4a, 4b and 4c, which show graphite surfaces bombarded at temperatures of 300K (ambient), 600K and 900K, respectively, using the intermediate flux J_2 and fluence Q_2 . From Fig. 4b we see that raising the sample temperature T to 600K produced surfaces which had roughly the same heights ($10 - 20$ Å) as those

produced at ambient conditions, but the characteristic wavelengths of the features were longer. Fig. 4c shows that a further increase in sample temperature to $T = 900\text{K}$ resulted in significantly smoother surfaces. For these conditions, the heights of the features were observed to be only 3 - 5 Å.

As mentioned above, topographs were acquired at many different image sizes for each surface. This is important for several reasons. To eliminate the possibilities of tip artifacts and problems with mechanical noise, it is critical to make certain that the features observed in larger images scale properly as the scan size is reduced. In addition, the STM is able to probe the small scale structures more accurately at the smaller scan sizes. This is a result of the maximum data density of 118 points per scan line and of the fact that, for constant scanning frequency, the tip velocity decreases as the image size is reduced, allowing more time for the STM to respond to the the surface topography. While it is impractical to present all topographs taken at different sizes, it is useful to examine a representative sampling. Therefore, images taken at scan sizes of $1000\text{ Å} \times 1000\text{ Å}$, $250\text{ Å} \times 250\text{ Å}$ and $50\text{ Å} \times 50\text{ Å}$ are shown in Figs. 5, 6 and 7 for the surfaces imaged at a size of $2400\text{ Å} \times 2400\text{ Å}$ in Figs. 1a, 2c and 3b, respectively. These surfaces represent the limits of roughness in the data set: one relatively smooth (Fig. 1a), one with large amplitude, short wavelength features (Fig. 2c) and one with large structures at large separations (Fig. 3b). The structures imaged at low magnification ($2400\text{ Å} \times 2400\text{ Å}$) in Figs. 1 - 3 are seen to scale properly down to the $250\text{ Å} \times 250\text{ Å}$ image size in figs. 5 - 7, confirming the size measurements of these features. In addition, if the scale for the image was reduced enough, the surfaces eventually appeared to be smooth (note that all topographs have been leveled, so a region that was on the side of a hillock is shown as flat), as observed in Figs. 5c, 6c and 7c at an image size of $50\text{ Å} \times 50\text{ Å}$.

In summary, it is apparent from this set of STM images that the nonequilibrium surfaces resulting from the sputtering of cleaved graphite substrates are strongly dependent on the bombardment conditions. For the lower fluences, the height of the features on the sputtered surfaces increased approximately linearly with increasing flux J . In addition, for each ion flux investigated, the surface morphology depended strongly on fluence Q . In general, short wavelength features were produced at the lowest fluence while the features increased in amplitude and separation as Q was increased. Sputter etching produced progressively smoother surfaces with increasing sample temperature. Finally, an investigation of images of bombarded graphite taken at various magnifications indicated that surface features scaled correctly as the image size was reduced, confirming the reliability of the data at large and small scan sizes. This scaling investigation also revealed that all of the sputtered surfaces began to appear smooth at an image size of $\sim 50 \times 50 \text{ \AA}^2$.

IV. Quantitative Analyses

The STM topographs clearly show trends in surface morphology as the sputtering parameters are varied and allow qualitative comparisons of surface roughness between the samples. The value of tunneling microscopy for this study, however, lies in the ability to calculate from the height data in the topographs the statistical functions that *quantitatively* describe the scaling behavior of the surface profiles. The quantities calculated for the graphite surfaces in this study are the corrugation, the auto-covariance function and the height correlation function.

The corrugation σ is the standard deviation of the surface slope and is calculated as a function of lateral length for distances of $2 - 100\%$ of the image size. The corrugation values are used to check for tip imaging artifacts in the

topographs. A large value of σ at a particular length would indicate that, at that separation, the protrusions and depressions on the surface have aspect ratios similar to the tunneling tip and that they can effectively act to image topography on the sides of the tip. This would produce an image which is a complicated convolution of the tip shape and the actual surface profile. Small values of the corrugation confirm that the tip is sharp compared to surface details and that the STM is able to probe the features correctly, producing an image that accurately represents the true topography. As an example, consider the saw-tooth shaped surface profile with features of height L shown in Fig. 8. At the lateral length scale of L , the slopes of the sides of the features are $+1$ and -1 , the average slope is zero and the corrugation σ is 1. The apex angle of each feature is 90° , indicating that for $\sigma = 1$, a reasonable tunneling tip should be able to accurately probe this artificial surface profile without serious convolution of the tip shape into the image, except at the concave corners. Our experience has shown that σ values less than 1.0 do not produce serious tip artifacts.

The topographs of rough or random surfaces contain an overabundance of information, making it difficult to pick out important trends and subtle features. To aid in the data analysis, we have calculated from the STM topographs the autocovariance functions $G(L)$, given by Eq. (1), and the height correlation functions $\langle |h(\mathbf{q})|^2 \rangle$, given by Eq. (2). These calculations serve to compress the data into a more useful and interpretable format, allowing quantitative determinations of the scaling behavior of the sputtered surfaces. It is instructive to first calculate these quantities for two limiting cases, a periodic surface and a totally random surface. The periodic surface, shown in Fig. 9a, is a high magnification atomic resolution image of graphite, collected at a size of $40 \text{ \AA} \times 40 \text{ \AA}$. The random surface topograph, shown in Fig. 9b, was produced by substituting the signal from a random noise generator⁴¹ for the tunneling microscope signal and allowing the

STM data acquisition system to collect the data as usual. To facilitate the comparison, the random surface image was also acquired at the $40 \text{ \AA} \times 40 \text{ \AA}$ size. The size of these images is actually irrelevant, as the results can be generalized to images of any size.

Autocovariance functions for these limiting surfaces are shown in Fig. 10a. In general, G probes the correlation of surface features as a function of separation distance, with nonzero values indicating correlated structures. Thus, $G(L)$ takes on positive and negative values and shows a periodic signature for the periodic features in the atomic resolution image of Fig. 9a. For the random surface of Fig. 9b, in which the data points are completely uncorrelated, $G = 0$ for all lengths except $L = 0$. The large peak in G at the origin is the variance of the height values. It is important to note that the number of data points used to calculate $G(L)$ decreases linearly as L increases, thus there is greater uncertainty in the autocovariance function at large L . This is not critical, however, because the large L regime will not be used in the analysis.

The height correlation function $\langle |h(q)|^2 \rangle$ is the Fourier transform of G and displays the scaling behavior of the surfaces as a function of wavevector q . The sample average $\langle \dots \rangle$ is performed by rotationally averaging $|h(q)|^2$ to obtain the radial part of the correlation function. As shown in Fig. 10b, the correlation function for the periodic surface clearly shows peaks at 2.2 \AA^{-1} and 2.8 \AA^{-1} superimposed on a sloping background. These peaks correspond to the atomic features with spacings of $2.24 - 2.86 \text{ \AA}$ seen in the topograph in Fig. 9a. As expected, $\langle |h(q)|^2 \rangle$ vs. q is roughly constant for the random surface in Fig. 9b, indicating that surface features are present at all wavevectors at approximately the same height. Note also that since the sampling accuracy of the Fourier transform decreases for features that approach the image size in real space, the

uncertainty in the correlation function is greatest for small values of the wavenumber q , which correspond to these lengths.

A. Surface Corrugation

Plots of the corrugation vs. lateral distance for three $2400 \text{ \AA} \times 2400 \text{ \AA}$ images, Figs. 1a, 2c and 3b, are shown in Fig. 11a. As mentioned previously, these surfaces make up a representative sampling of the extremes of the data. The corrugations for these surfaces are all less than 0.7 for length scales down to $\sim 40 \text{ \AA}$, which indicates structures with apex angles greater than 110° at these length scales. The topographs in Figs. 1 - 4 *appear* much rougher than this because the length scale for the Z - axis is highly expanded relative to the X - and Y - axes. As a more careful check of image reliability at lengths less than 50 \AA , the corrugations for high magnification images (Figs. 5c, 6c and 7c) of these same representative surfaces are shown in Fig. 11b. In some cases, this resulted in higher values of σ for these high magnification images as the length scale approached zero.

Very blunt tips could also produce images with small values of σ because the tip would not be able to follow sharp features. For the tips used to image rough surfaces in this study, however, atomic resolution images of clean graphite were also obtained, indicating the tips were $\leq 9 \text{ \AA}$ in diameter.³⁰ At the length scales for the topographs presented in Figs. 1-4, this tip width is negligible.

Similar results for the corrugation were found for all surfaces in this study except the high magnification images of the surface shown in Fig. 1c. This sample, which was sputtered with the highest flux (J_3) and the lowest fluence (Q_1), had values for σ that approached 15 for lengths smaller than 10 \AA , indicating that these images most likely had some tip artifacts at small lateral distances.

B. Auto-covariance function

For the rough surfaces in this study, useful information can be extracted from the auto-covariance function $G(L)$ given by Eq. (1) if certain simplifying assumptions are made. Because the mathematical function that describes the real space profile of a rough surface is unknown and difficult to find, one usually assumes that this profile represents a stochastic process that can be described by a probability distribution function.²⁴ Thus, the surface profile can be characterized by a knowledge of the moments of the distribution function. If we assume a Gaussian probability function, then the rough surfaces measured here can be characterized by the root-mean-square (rms) surface height and the $1/e$ width of the auto-covariance function, called the auto-covariance length. Since the data in the topographs are fitted to a plane to remove any tilt in the image, the mean height of the surface, $\langle h(r) \rangle \sim 0$. This leaves the auto-covariance function $G(L)$ with behavior for small L that can be approximated as:

$$G(L) = \delta^2 \exp(-L^2/\lambda^2), \quad (3)$$

where the interface width $\delta \equiv \sqrt{G(0)}$ is the rms surface height and the auto-covariance length λ is the short range measure of the lateral correlation of the surface features.

For the topographs of sputtered graphite, the auto-covariance functions were determined both parallel and perpendicular to the fast scanning direction of the STM, providing a check on the isotropy of the images. Significant differences in $G(L)$ along these two directions would indicate an asymmetry in the tip or the roughening of the surface. For this set of data, however, no significant differences were seen for the two orientations of the auto-covariance functions. Therefore, $G(L)$ is shown only perpendicular to the direction of scanning.

Table I gives the values of λ and δ for the images in Figs. 1 - 3. In addition, plots of $G(L)$ vs. L for some of the surfaces of Figs. 1 - 3 are shown in Fig. 12. The initial regions in these plots have been approximated as Gaussian in shape to permit the extraction of an interface width and auto-covariance length. For the lowest fluence Q_1 , the behavior of G with increasing flux is shown in Figs. 12a, 12b and 12c, corresponding to the surfaces in Figs. 1a, 1b and 1c, respectively. The fact that $\lambda > 0$ means that the features produced by the ion bombardment are not random, as one might expect, but are *correlated*. The auto-covariance length λ was approximately constant for the two lower fluxes but decreased to 20 Å for the highest flux, at which the $G(L)$ vs. L curve now looks more like that in Fig. 10a for the random noise surface. The values of the interface width δ for these curves increased with increasing flux, in the ratio of 1 : 3.3 : 20, compared to the flux ratio of 1 : 5 : 10. From Table I, we observe similar behavior with increasing flux J for the intermediate fluence Q_2 : λ decreased steadily as J was increased and the interface width δ increased, albeit more slowly than for the lowest fluence, with the ratio 1 : 2.1 : 3.4. These trends in the parameters λ and δ for the low and intermediate Q quantify the increasing dominance of short range roughness and illustrate the increase in the random nature of the surfaces as the ion flux is increased. The values in the third column of Table I, representing the highest fluence Q_3 , do not follow the trends seen for lower fluences. We see here that the surface with the largest δ was produced at the intermediate flux.

Figs. 12a, 12d and 12e show the behavior of the auto-covariance function as the fluence is increased at the lowest flux J_1 , and correspond to the images in Figs. 1a, 2a and 3a, respectively. For these surfaces, the auto-covariance length increased by ~100 Å for each tenfold increase in the fluence Q , indicating the formation of features at larger separation. The structures also increased rapidly in size, as seen in the dramatic increase of interface width δ in the ratio of 1 : 3.9 :

43, for fluences that increased in the ratio 1 : 10 : 100. The second row in Table I shows similar results for λ and δ at the intermediate flux J_2 , although the increase in the interface width was more moderate, with a ratio of 1 : 2.5 : 28. For surfaces sputtered at the highest flux J_3 , the behavior of $G(L)$ with increasing Q is quite different. The value of λ was roughly constant between the low and intermediate fluences but increased abruptly at the highest Q . The interface widths indicate that the surface is smoothest for the intermediate value of Q . This behavior may have resulted from the experimental difficulties in controlling the sputtering time, and hence the fluence, for the surface etched at the highest flux (J_3) and the smallest fluence (Q_1).

It is especially interesting to compare the rates of increase of δ discussed above with a crude estimate of the interface width which neglects the presence of any smoothing mechanisms. In reality, some smoothing is expected, thus this simplistic model should overestimate the roughness produced. If we assume individual ion/surface impacts to be independent of each other, we would expect a random surface similar to that shown in Fig. 9b, for which $\lambda \approx 0$. As the fluence Q is increased, δ would increase as well, but the surface would remain random in character. The arrival of ions, and hence the removal of material from the surface, is assumed to be governed by Poisson statistics, for which the standard deviation in $h(r)$ is given by the square root of the amount of material sputtered from the surface. The interface width δ should be approximately proportional to this quantity, with the interplanar spacing as the proportionality constant, resulting in:

$$\delta = d\sqrt{QY/\rho}, \quad (4)$$

where Y is the sputtering yield, taken to be 1.5 here, ρ is the monolayer area density (3.8×10^{15} atoms/cm²) and d ($= 3.35$ Å) is the interlayer spacing for graphite. The results of this estimate for the three fluences used in these experiments are also given in Table I and have the ratio 1 : 3.2 : 10. It is clear from the ratios presented above that the roughness increased with fluence more rapidly than the $Q^{1/2}$ dependence of this crude estimate of δ . This behavior is quite unexpected, and indicates that there is some mechanism *in addition* to shot noise that is roughening the bombarded surfaces at high Q . In other words, the individual sputtering events are not independent of each other but are *correlated* in some way, so the surface retained a memory of previous ion impacts.

Plots of the auto-covariance function $G(L)$ for the surfaces sputtered at different temperatures (Fig. 4) are shown in Fig. 13. There was a marked decrease in the interface width δ as the temperature was increased. In addition, the auto-covariance length λ decreased as well, from 100 Å to 35 Å, but only for the highest temperature used (900K). These values quantify the decrease of the short scale roughness seen in the images of Fig. 4 but give little information about changes in long range correlations.

The auto-covariance function G provided a framework for a quantitative analysis of rough surfaces in real space. It was useful in demonstrating the existence of a surface memory effect, in extracting values for the short range correlations given by the auto-covariance length λ , and in quantifying the roughness of the sputtered surfaces given by the interface width δ . As seen in Table I, the trends in these parameters can be related to changes in the flux, ion fluence and sample temperature, and agree with the qualitative trends observed in the topographs of Figs. 1 - 4. In particular, the behavior of the interface width as the fluence Q is varied indicates the existence of a roughening mechanism for sputtered graphite in addition to shot noise. The utility of the real space auto-

covariance function is limited, however, because the assumption of Gaussian behavior for $G(L)$ vs. L is followed only approximately by the sputtered graphite surfaces and there is no detailed theory relating the observables to the surface formation processes.

C. Height correlation function

A very useful complementary view of the scaling behavior of the sputtered surfaces was obtained by using Eq. (2) to calculate from the topographs the height correlation function as a function of the wavenumber q . The required sample average $\langle |h(q)|^2 \rangle$ was obtained by performing a rotational average of the two-dimensional $|h(q)|^2$ function. For each value of q , $|h(q)|^2$ was sampled at angular increments of 1° and averaged over a range of 180° . Because it is symmetric, only half of the Fourier transform was needed for the calculation. The variance of $\langle |h(q)|^2 \rangle$ was also calculated to provide an estimate of the uncertainty in the correlation function.

Figs. 14 - 17 show plots of $\langle |h(q)|^2 \rangle$ vs. q calculated from the topographs in Figs. 1 - 7. The general behavior of the correlation functions for bombarded surfaces is clearly different from that shown in Fig. 10b for either the random or the periodic surfaces, again indicating that the stochastic process of ion bombardment has produced surfaces that are neither random nor periodic, but are correlated. The scaling behavior of features on these surfaces can be quantified by determining the correlation length ξ and the functional dependence of $\langle |h(q)|^2 \rangle$ vs. q . The corrugation σ can be used to visualize the meaning of ξ in real space. As observed in Fig. 11, the corrugation of each surface becomes small for points separated by lengths larger than ξ . Thus, for such length scales, the surface can be considered to be flat. For this real space behavior, one would expect that the height correlation function should be q -independent for $q \leq 2\pi/\xi$,

while it should decrease with q for $q \geq 2\pi/\xi$. This signature of correlation is clearly seen in the curves of Figs. 14 -17.

The creation of correlated structures by particle radiation appears to be counter-intuitive. However, theoretical studies of the non-equilibrium growth of interfaces^{20,21} indicate that correlation resulting from random events is possible. From linear response theory for the case of isotropic radiation erosion, the general form of the continuum differential equation describing the evolution of the surface profile as a function of time and position is^{42,43}:

$$\frac{\partial h}{\partial t} \propto -D_s \nabla^4 h - D_v \nabla^3 h - \gamma \nabla^2 h - J\theta(r, (h)) + \eta(r, t). \quad (5)$$

The first four terms, which represent the smoothing mechanisms of surface diffusion, volume diffusion, sputter redeposition and sputter removal affected by shadowing, respectively, are illustrated schematically in Fig. 18. The diffusion terms describe annealing by flow of material along the surface or through the bulk. The sputter redeposition term describes removal of material by sputtering and subsequent recondensation at a different place on the surface. The sputter removal term incorporates the dependence on exposure angle θ . This so-called 'shadowing' term accounts for the preferential erosion of the tops of prominent features due to their increased exposure to the incoming flux.⁴⁴ The final term $\eta(r, t)$ is the Gaussian white noise for the incident ions with a variance proportional to the flux J and represents the only surface roughening mechanism in the theory.

A simplified linear response argument was proposed for radiation erosion in Ref. 44 and compared to a subset of our data in Ref. 45. Since $D_s \gg D_v$, i.e. the surface diffusion constant is always much larger than that for the bulk, the volume diffusion term was neglected. In addition, sputter redeposition was also

assumed to be small in Ref. 45, but has been explicitly included here. The resulting continuum differential equation is:

$$\frac{\partial h}{\partial t} = -D\nabla^4 h - \gamma\nabla^2 h - J\theta(r, h) + \eta(r, t). \quad (6)$$

where D is proportional to the surface diffusion constant and γ contains a constant characteristic of the material. Fourier analysis of Eq. (6) leads to:

$$\frac{\partial h(\mathbf{q}, t)}{\partial t} = -\omega(\mathbf{q}) h(\mathbf{q}, t) + \eta(\mathbf{q}, t), \quad (7)$$

where the three smoothing terms have been grouped together in $\omega(\mathbf{q})$, the healing rate of a surface modulation of wavevector \mathbf{q} :

$$\omega(\mathbf{q}) \propto J|\mathbf{q}| + \gamma|\mathbf{q}|^2 + D|\mathbf{q}|^4. \quad (8)$$

The resulting reciprocal space correlation function is

$$\langle |h(\mathbf{q})|^2 \rangle_t \propto \frac{J}{\omega(\mathbf{q})} [1 - \exp(-2\omega(\mathbf{q})t)]. \quad (9)$$

According to Eq. (9), for small \mathbf{q} , $\langle |h(\mathbf{q})|^2 \rangle_t$ is independent of \mathbf{q} , while for large \mathbf{q} it should decrease with \mathbf{q} , indicating two distinct regions in plots of $\langle |h(\mathbf{q})|^2 \rangle_t$ vs. \mathbf{q} . Figs. 14 - 17 show that this general behavior is exactly what was seen in the experimentally determined correlation functions.

Fig. 14 shows the dependence of the correlation function on flux J , for fixed fluence Q . The crossover wavevector $q_0 = 2\pi/\xi$, which marks the transition in the behavior of $\langle |h(\mathbf{q})|^2 \rangle$ from a constant to a decreasing function of \mathbf{q} , is defined by $\omega(q_0)t = 1$. Eq. (8) predicts that the correlation length at crossover, $\xi \propto Q = Jt$, assuming $\xi \leq (D/J)^{1/3}$, and thus that q_0 should remain constant for the correlation functions in Fig. 14a and in Fig. 14b, which correspond to the lower fluences Q_1 and Q_2 , respectively. This behavior is seen for the two lower curves of Fig. 14a, which correspond to fluxes J_1 and J_2 . In the upper curve, however,

which represents the highest flux J_3 , q_0 has increased. In Fig. 14b, q_0 also increased with increasing flux, albeit rather slowly. These trends can also be seen from the values of ξ , calculated from the crossover wavevectors, given in Table I. To investigate the behavior of the correlation function for the limit $q \rightarrow 0$, the exponential term in Eq. (9) can be expanded and gives the result $\lim_{q \rightarrow 0} \langle |h(q)|^2 \rangle_t \propto Jt = Q$, indicating that the curves in Fig. 14a and Fig. 14b, for which Q is constant, should all converge to the same point in the small q limit. This result is *independent* of our choice of the healing rate function, $\omega(q)$, as long as $\omega(q) \rightarrow 0$ as $q \rightarrow 0$. Within the experimental uncertainty, this is true for the curves corresponding to fluxes J_1 and J_2 in Fig. 14a and for the curves corresponding to fluxes J_2 and J_3 in Fig. 14b.

For very large q , $\omega(q) \propto Dq^4$, and from Eq. (8) we have $\lim_{q \rightarrow \infty} \langle |h(q)|^2 \rangle_t \propto J/(Dq^4)$. This predicts that the log/log plots of $\langle |h(q)|^2 \rangle_t$ shown in Fig. 14a should be straight lines with slopes of -4 for large enough q and should be separated from each other vertically by amounts which scale linearly with the fluxes, which are in the ratio of 1 : 5 : 10. The three curves all appear to have roughly the same slope, but the q dependence is between $q^{-2.5}$ and $q^{-2.9}$, and the vertical separations of $\langle |h(q)|^2 \rangle_t$ curves at large q follow the ratio 1 : 10 : 400 in Fig. 14a and 1 : 10 : 100 in Fig. 14b. Thus, over the range of q in the plots of Figs. 14a and 14b, both surface diffusion ($\propto q^{-4}$) and sputter redeposition ($\propto q^{-2}$) contribute significantly to the healing function $\omega(q)$. The importance of sputter redeposition has also been demonstrated by STM studies of single ion impacts,^{46,47} which have shown considerable transport of material in the vicinity of impact sites.

The behavior of the correlation functions as Q is varied is shown in Fig. 15. Although Eq. (9) predicts the correlation length ξ to be proportional to the fluence, we find from the data in Figs. 15a and 15b, for the fluxes J_1 and J_2 , respectively, and from the calculated values of ξ in Table I, that the correlation length

increases more slowly than linearly with Q for all fluxes investigated. In addition, we can define a long-wavelength interface width W from the height correlation functions as $W = \lim_{q \rightarrow 0} (\langle |h(q)|^2 \rangle_t)^{1/2} \propto (Jt)^{1/2} = Q^{1/2}$. This asymptotic limit of the linear response theory represents the solution of Eq. (6) with no smoothing mechanisms and corresponds to the previous estimate from Eq. (4) of the expected interface width δ in the auto-covariance function. For the data in Figs. 15a and 15b, Q was increased in the ratio 1 : 10 : 100 from the lowest to the highest curves. For a $Q^{1/2}$ dependence, we expect the interface width W to increase as 1 : 3.1 : 10. We see from Table I that for the two lower fluxes J_1 and J_2 , W increased in the ratios 1 : 9.5 : 124 and 1 : 11 : 325, respectively, a dependence more like Q than $Q^{1/2}$. As in the analysis of the auto-covariance function, this behavior shows that the surface roughening from bombardment exceeds even the predictions of a model with only a *stochastic roughening* mechanism included. This remarkable result, which violates the linear response theory of Ref. 44, is direct evidence that a simple linear theory cannot explain the nonequilibrium surfaces produced by the sputtering of amorphous carbon.

For the highest etching flux, J_3 , the interface width W increased with Q in the ratio 1 : 3.4 : 7.5, which is closer to a $Q^{1/2}$ dependence. This suggests that any nonlinear roughening mechanism for the two lower fluxes is no longer dominant at the highest flux. The energy deposition rate into the surface was the highest for this value of the flux, which means that localized heating by the ion collisions with the surface may be significant. Calculations of the thermal spike,⁴⁸ the local increase in temperature caused by a collision of a 5 keV argon ion with the surface, indicate temperatures of ~ 660 K in the vicinity of an impact site. As already observed, this temperature is enough to cause some enhancement in the surface diffusion at the smaller length scales. Compared to the lower fluxes, at the highest value J_3 the impacts with the surface occur closer in time and spatial

separation, possibly allowing enhanced surface diffusion to effectively smooth out the extreme roughening observed at the lower fluxes. Finally, for large fluences (ie. long times) and $q \gg 0$, the exponential term in Eq. (9) can be neglected, making $\langle |h(q)|^2 \rangle_t$ independent of Q . The experimental results shown in Figs. 15a and 15b, however, indicate a significant Q dependence of the correlation function at large wavevector for the range of fluences studied.

As a final test of Eq. (9), we investigated the behavior of the correlation function $\langle |h(q)|^2 \rangle_t$ for sputtering experiments performed at elevated temperatures. Plots of $\langle |h(q)|^2 \rangle_t$ calculated from the topographs in Fig. 4 are shown in Fig. 16. These surfaces were all bombarded at the intermediate flux and fluence (J_2 and Q_2) but at progressively higher temperatures. Above 600°K, $\langle |h(q)|^2 \rangle$ drops more sharply with q and, for large q , has a tail with an approximate q^{-4} dependence, which demonstrates that surface diffusion dominates the healing function at the higher temperatures.

While the general trends in the experimental data are consistent with Eq. (9), the quantitative comparisons above rule out the strict validity of the linear response theory of Eq. (6) for ion etched graphite over the range of parameters that we investigated. A roughening mechanism besides shot noise is required to account for the Q dependence of the roughening observed on sputtered graphite. This means that Eq. (6) must have another positive term, perhaps one that is proportional to h^2 or $(\nabla h)^2$

At present, no non-linear theory exists for radiation erosion, but a general scaling description²¹ has been developed in the context of various growth models.²⁰ Analysis of the scaling behavior of the data may provide clues to the mechanism for surface roughening of ion bombarded graphite. According to this scaling theory:⁴⁵

$$\langle |h(q)|^2 \rangle_t \propto q^{-\nu} F(t q^2), \quad (10)$$

with $F(x) \propto x^{\nu/2}$ for small x , and $F(x) \sim \text{constant}$ for large x . This would predict a power law decrease, $q^{-\nu}$, in $\langle |h(q)|^2 \rangle_t$ for $q \geq t^{-1/2}$.

In Figs. 14 and 15, the correlation functions calculated from $2400 \text{ \AA} \times 2400 \text{ \AA}$ images show an approximate power law dependence at large q with an associated exponent $-\nu$ of order -2.5 to -2.9 . Because of the limitations on the data density in the topographs, however, the behavior of $\langle |h(q)|^2 \rangle_t$ can only be plotted up to $q \sim 0.2 \text{ \AA}^{-1}$ for these images. The range of q can be extended to larger values, however, by overlapping the correlation functions calculated for images of increasingly smaller scan size. This was done in Fig. 17 with $\langle |h(q)|^2 \rangle_t$ curves calculated from the topographs in Figs. 5 - 7, which have sizes of $1000 \text{ \AA} \times 1000 \text{ \AA}$, $250 \text{ \AA} \times 250 \text{ \AA}$ and $50 \text{ \AA} \times 50 \text{ \AA}$, and the correlation functions computed from the corresponding $2400 \text{ \AA} \times 2400 \text{ \AA}$ images. The plots of $\langle |h(q)|^2 \rangle_t$ for these three surfaces extend over four decades in wavenumber q . In most cases the correlation function curves overlap quite well with each other. The discontinuity between some of the curves of differing image sizes may be caused by the fact that each image was leveled before the power spectrum was computed, which can introduce small vertical scale shifts. This results in slightly higher values of $\langle |h(q)|^2 \rangle_t$ from the smaller images. For the majority of the correlation functions in Fig. 17, however, the curves do overlap within the error bars, shown in Figs. 14 and 15, which indicate an uncertainty of plus or minus one standard deviation. More significantly, the *slopes* of the curves at large q agree with those calculated at smaller q from the low magnification images, indicating that the scaling behavior observed in the correlation functions from large images (distances $> 2000 \text{ \AA}$) is consistent down to length scales $< 50 \text{ \AA}$, where the surfaces begin to appear smooth. The position of the crossover wavevector q_0 is approximately the same in

curves of the correlation function computed from images of different magnifications.

Under conditions of rotational invariance, the exponent z in Eq. (10) is related to ν by $z = 2 - \alpha$, with $2\alpha = \nu - 2$. From the experimentally determined correlation functions, $\nu \sim 2.5 - 2.9$, resulting in $z \sim 1.6 - 1.8$ and $\nu/z \sim 1.5$. This would mean that for small q , $\langle |h(q)|^2 \rangle_t \sim t^{\nu/z}$ should increase *faster* than linearly with increasing time (fluence), while the correlation length at crossover, $\xi \sim t^{1/z}$, should increase *more slowly* than linearly. As we have seen earlier, both functional dependences were observed for the experiments in this study. The values of α obtained from numerical studies in three dimensions are model dependent:⁴⁹ for weak non-linearity, α values in the range 0.15 - 0.23 were reported, while α is ~ 0.4 for strong coupling. For our experiments, we find α to be $\sim 0.2 - 0.4$. The results embodied in Figs. 14 and 15 thus appear to be consistent with local growth models, at least at the lower fluences. This demonstrates that there is a strong connection between the morphologies of surfaces formed by vapor deposition and by erosion via sputtering.⁴⁴

V. Conclusions

Our STM examinations of highly oriented pyrolytic graphite eroded by ion beam sputter etching revealed a number of dramatic trends in surface roughness as the bombardment parameters of ion flux, fluence and temperature were varied. For the lower fluences, we observed a steady increase in roughness as the ion flux was increased, with a corresponding decrease in the separation (wavelength) of the surface features. We were also able to follow the evolution of the surface morphology as the ion fluence was increased. Regardless of the ion flux used, for small fluences the initially flat surfaces showed short wavelength roughness which evolved into much larger structures separated by distances

which exceeded the image size ($2400 \text{ \AA} \times 2400 \text{ \AA}$) as the bombardment was continued. The fact that roughness is produced at all from the atomically flat, cleaved graphite surfaces is significant in itself, confirming that the shot noise in the incoming ion flux acts as a roughening mechanism at the length scales investigated here. Because of enhanced surface diffusion, sputtering at elevated temperatures produced surfaces which were significantly smoother than those bombarded at ambient conditions. This smoothing effect was most dramatic for $T > 600\text{K}$.

Observations from the STM topographs themselves clearly show these trends, but only in a qualitative manner. It is clearly impossible to extract much quantitative information about the distribution of length scales on the bombarded surfaces by visual examination of the topographs alone. In fact, to the inexperienced observer, many of the surfaces produced by sputter etching have a random appearance. We therefore relied on the auto-covariance function $G(L)$ in real space, and the height correlation function $\langle |h(\mathbf{q})|^2 \rangle$ in reciprocal space, to provide a quantitative statistical description of the scaling and correlation of the sputtered surfaces. Both analyses show conclusively that, while the atomic ordering of the cleaved graphite surfaces was obliterated by the argon ion bombardment, the resulting surfaces were not at all random in nature. On the contrary, they exhibited correlated behavior which scaled with wavenumber q in a well determined fashion. Since ion bombardment is a stochastic process, visualized as random impacts in time and space at these length scales, there are other processes that are important in determining the surface morphology.

The most significant result from the auto-covariance function analysis was that the increase in the interface width δ with increasing fluence at the lower fluxes was greater than expected from a simple surface damage estimate, indicating another roughening mechanism in addition to shot noise. At the lower

fluences, the decreasing values of the auto-covariance length λ with increasing flux suggest that the surfaces evolved topography with scaling similar to that of a random surface.

The reciprocal space analysis of the roughened surfaces, using the height correlation function $\langle |h(q)|^2 \rangle_t$, was the most useful for making comparisons to theories of surface erosion by sputtering. A linear response theory for sputter erosion was compared to the experimental data. This model incorporates the smoothing actions of shadowing, sputter redeposition and surface diffusion, and the roughening mechanism of shot noise, which describes the variation of the incident ion flux around some mean value. Several of the predictions of the model were satisfied by the experimental results, namely that the correlation function $\langle |h(q)|^2 \rangle$ should be independent of q up to some crossover wavevector q_0 , after which the curve should decrease as some negative power of q . For large q the theory predicts a q dependence somewhere between q^{-2} and q^{-4} . The experimental correlation functions for samples sputtered at ambient temperature decrease as $\sim q^{-2.7}$, which demonstrates that both sputter redeposition and surface diffusion contribute to the surface annealing. For sputtering at $T = 900$ K, the correlation function has a distinct q^{-4} tail at large q , which demonstrates that surface diffusion has become the dominant annealing mechanism.

However, a further comparison of the experimental data to the linear theory revealed several discrepancies. At the lowest fluence Q , the independence of the correlation length $\xi = 2\pi/q_0$ with respect to flux J is roughly obeyed for the two lower fluxes, but not for the highest value J_3 . At intermediate Q , ξ increases slowly with J . For constant flux, a linear dependence of ξ on Q is expected, but we find that the correlation length increases more slowly than linearly with Q for all fluxes investigated. The linear response argument predicts the long-wavelength interface width W calculated from the correlation functions to be proportional to

$Q^{1/2}$ in the limit $q \rightarrow 0$. Instead, for the lower fluxes we see that W is essentially proportional to Q , indicating the existence of a roughening mechanism in addition to shot noise. This enhanced roughening behavior suggests that individual sputtering events are no longer independent but are correlated in some way. At higher flux, this roughening effect is compensated. At large wavevector q , linear response arguments predict $\langle |h(q)|^2 \rangle$ to be independent of Q while experimental results indicated a significant fluence dependence. Theoretically, the vertical separation of the $\langle |h(q)|^2 \rangle$ curves should scale linearly with the flux J for fixed Q , but the separations for constant Q increase more quickly than linearly.

The linear response theory does not quantitatively describe the sputtering of graphite for the conditions investigated here. To model the enhanced roughening seen at the lower fluences, Eq. (6) must be modified with a new term proportional to h^n or $(\nabla h)^n$, where $n > 1$. Unfortunately, there is no analytical solution for such an equation. At present, we have no explanation for the physical mechanism that would produce such a term.

The fact that the experimental results were consistent with a general scaling theory applicable to the evolution of nonequilibrium surfaces is encouraging. The power law decrease in the correlation functions at large q seen in the experimental data has an associated exponent of -2.5 to -2.9, which is consistent with a weak nonlinearity. This behavior extends over several decades in q , as seen from the correlation functions calculated from high magnification images. In addition, the scaling theory is also consistent with a slower than linear increase in the correlation length ξ with increasing fluence and a faster than linear increase of the correlation function with fluence at small q .

In general, the experiments in this study demonstrate the utility of the scanning tunneling microscope as a tool for studying the topography of rough

surfaces. The analyses presented here define a comprehensive framework for the quantitative analysis of surface topography produced by any of the various erosion and deposition techniques currently in use. In this study, computations of the correlation functions allowed us to investigate the statistical behavior of the roughness which developed on sputtered graphite surfaces. It was then possible to make detailed comparisons to theoretical descriptions and to find evidence for a number of surprising phenomena produced by sputter erosion.

The exploration of a larger volume of the parameter space of sputtering variables is now required. For example, it is necessary to extend the ion fluence Q to higher values to see if the enhanced roughening effect continues to dominate. Also, we have yet to determine the effects on the sub-micron scale topography of sputtered graphite of varying other parameters such as the energy of the incoming ions and the incidence angle. Finally, the effects of ion bombardment at these small length scales on materials other than graphite must be investigated. Quantitative analysis of the resulting surface morphologies under the framework developed in this study will allow us to make further inroads into the understanding of the basic physics of sputter etching and deposition, and eventually make it possible to predict the scaling behavior of the resulting surfaces from the initial sputtering conditions.

VI. Acknowledgements

This work was supported by the National Science Foundation through Grant DMR 8922027 and by the Office of Naval Research. We would like to thank R. Bruinsma, J. Rudnick and R.P.U. Karunasiri for their assistance with the theoretical analysis.

References

1. J. L. Vossen and W. Kern, *Thin-Film Processes* (Academic Press, New York: 1978).
2. H. J. Mathieu, in *Thin Film and Depth Profile Analysis*, H. Oechsner, ed. (Springer-Verlag, Berlin: 1984), pp. 39-58.
3. G. Carter, in *Erosion and Growth of Solids Stimulated by Atom and Ion Beams*, G. Kiriakidis, G. Carter, and J. L. Whitton, eds. (Martinus Nijhoff, Hingham, MA: 1986), pp. 70-97.
4. I. J. Hodginson and P. W. Wilson, *CRC Reviews* **15**, 27 (1988).
5. O. Auciello, in *Ion Bombardment Modification of Surfaces*, O. Auciello and R. Kelly, eds. (Elsevier, Amsterdam: 1984), pp. 1-22.
6. D. P. Woodruff and T. A. Delchar, *Modern Techniques of Surface Science*, (Cambridge University Press, Cambridge: 1986), pp. 6-7.
7. S. Hoffman and J. M. Sanz, in *Thin Film and Depth Profile Analysis*, H. Oechsner, ed. (Springer-Verlag Berlin: 1984), pp. 141-156.
8. E. Cirlin, Y. T. Cheng, P. Ireland, and B. Clemens, *Surface and Interface Analysis*, **15**, 337 (1990).
9. G. W. Rubloff, *J. Vac. Sci. Tech.* **B 7** (6), 1454 (1989).
10. Y. Hirooka, R. W. Conn, T. Sketchley, W. K. Leung, G. Chevalier, R. Doerner, J. Elverum, D. M. Goebel, G. Gunner, M. Khandagle, B. Labombard, R. Lerner, P. Luong, Y. Ra, L. Schmitz and G. Tynan, *J. Vac. Sci. Tech.* **A 8** (3), 1790, (1990)
11. Part II, Composites, in *Carbon Fibers, Filaments and Composites*, J. L. Figueiredo, C. A. Bernardo, R. T. K. Baker and K. J. Huttinger, eds. (Kluwer Academic Publishers, Dordrecht: 1990), pp. 169 - 404.

12. See, for example, G. Carter and M. J. Nobes, *Earth Surface Process* **5**, 131 (1980).
13. T. Marsh and R. Collins, *Rad. Effects* **99**, 171 (1986).
14. I. V. Katardjiev, *J. Vac. Sci. Technol. A* **6** (4), 2434 (1988).
15. J. A. Kubby and B. M. Siegel, in *Erosion and Growth of Solids Stimulated by Atom and Ion Beams*, G. Kiriakidis, G. Carter, and J. L. Whitton, eds. (Martinus Nijhoff, Hingham, MA: 1986), pp. 444-452.
16. See, for example, D. M. Mattox, *J. Vac. Sci. Technol. A* **7** (3) 1105 (1989).
17. G. Carter, B. Navinsek, and J. L. Whitton, in *Sputtering by Particle Bombardment, Vol. II*, R. Behrisch, ed. (Springer-Verlag, Berlin: 1983), pp. 231-266.
18. S. Sobue and F. Okuyama, *J. Vac. Sci. Technol. A* **8** (2), 785 (1990).
19. M. Tanemura and F. Okuyama, *Nucl. Instr. and Meth. in Phys. Res. B* **47**, 126 (1990).
20. M. Kardar, G. Parisi, and Y. C. Zhang, *Phys. Rev. Lett.* **56**, 889 (1986). For a review, see T. Vicsek, *Fractal Growth Phenomena* (World Scientific, Singapore: 1989).
21. F. Family and T. Vicsek, *J. Phys. A* **18**, L75 (1985).
22. P. K. Hansma and J. Tersoff, *J. Appl. Phys.* **61** (2), R1 (1987).
23. H. Rohrer, in *Scanning Tunneling Microscopy and Related Methods*, R. J. Behm, N. Garcia, and H. Rohrer, eds. (Kluwer Academic Publishers, Dordrecht: 1990), pp. 1-26.
24. M. Rasigni, G. Rasigni, F. Varnier, C. Dussert, J. Palmari, and N. Mayani, "Statistical Analysis of Rough and Random Surfaces", in *Surface Measurement and Characterization*, J. M. Bennett, ed., Proc. SPIE 1009, pp. 68-76 (1989).

25. J. D. Weeks, in *Ordering in Strongly Fluctuating Condensed Matter Systems* (Plenum, New York: 1980), pp. 293.
26. G. Reiss, J. Vancea, H. Wittman, J. Zweck, and H. Hoffman, *J. Appl. Phys.* **67** (3), 1156 (1990).
27. D. R. Denley, *J. Vac. Sci. Technol. A* **8** (1) 603 (1990).
28. C. Schönenberger, S. F. Alvarado, and C. Ortiz, *J. Appl. Phys.* **66** (9) 4258 (1989).
29. E. J. Snyder, E. A. Eklund, and R. S. Williams, *Surf. Sci. Lett.* **239** L487 (1990).
30. E. J. van Loenen, D. Dijkkamp, A. J. Hoeven, J. M. Lenssinck, and J. Dieleman, *Appl. Phys. Lett.* **56** (18) 1755 (1990).
31. G. Binnig, H. Fuchs, Ch. Gerber, H. Rohrer, E. Stoll, and E. Tosatti, *Europhysics Lett.* **1**, 31 (1986).
32. J. E. Demuth, R. J. Hamers, R. M. Tromp, and M. E. Welland, *J. Vac. Sci. Technol. A* **4** (3) 1320 (1986).
33. Ch. Cerber, G. Binnig, H. Fuchs, O. Marti, and H. Rohrer, *Rev. Sci. Instr.* **57**, 221 (1986).
34. J. Schneir, "Electronics for Tunneling Microscopy at UCSB", unpublished handout, P. K. Hansma Group, Dept. of Phys., Univ. of Calif., Santa Barbara, CA 93106.
35. A. Bryant, D. P. E. Smith, and C. F. Quate, *Appl. Phys. Lett.* **48** (13) 31 (1986).
36. J. L. Lauer and P. B. Abel, NASA Technical Memorandum 100299 (1988).
37. J. Garnaes, F. Kragh, K. A. Mørch and A. R. Thölén, *J. Vac. Sci. Technol. A* **8**(1) 441 (1990).
38. D. F. Ogletree, C. Ocal, B. Marchon, G. A. Somorjai, M. Salmeron, T. Beebe and W. Siekhaus, *J. Vac. Sci. Technol. A* **8** (1) 297 (1990).

39. M. R. Khan, N. Heiman, R. D. Fisher, S. Smith, M. Smallen, G. F. Hughes, K. Veirs, B. Marchon, D. F. Ogletree, M. Salmeron, and W. Siekhaus, *IEEE Trans. on Mag.*, **24** (6) 2647 (1988).
40. J. F. Ziegler, J. P. Biersack, and U. Littmark, *The Stopping and Range of Ions in Solids*, (Pergammon Press, New York: 1985).
41. Type 1390-B Random Noise Generator, made by General Radio Company, Concord, MA.
42. C. Herring, *J. Appl. Phys.* **21**, 301 (1950).
43. R.P.U. Karunasiri, PhD thesis, University of California Los Angeles, 1991.
44. G. S. Bales, R. Bruinsma, E. A. Eklund, R.P.U. Karunasiri, J. Rudnick, and A. Zangwill, *Science* **249**, 264 (1990).
45. E. A. Eklund, R. Bruinsma, J. Rudnick and R. S. Williams, submitted.
46. L. Porte, M. Phaner, G. H. de Villeneuve, N. Moncoffre, and J. Tousset, *Nucl. Inst. and Meth. in Phys. Res.* **B44** 116 (1989).
47. R. Coratger, A. Claverie, F. Ajustron, and J. Beauvillain, *Surf. Sci.* **227**, 7 (1990).
48. R. Kelly, in *Ion Bombardment Modification of Surfaces*, O. Auciello and R. Kelly, eds. (Elsevier, Amsterdam: 1984), pp. 53.
49. H. Yan, D. Kessler, and L. M. Sander, *Phys. Rev. Lett.* **64**, 926 (1990).

Figure Captions

- Fig. 1 Constant current STM topographs of graphite surfaces after sputter etching with an ion fluence of $Q_1 = 10^{16}$ ions/cm² and fluxes of (a) $J_1 = 6.9 \times 10^{13}$ ions/cm² sec, (b) $J_2 = 3.5 \times 10^{14}$ ions/cm² sec, and (c) $J_3 = 6.9 \times 10^{14}$ ions/cm² sec. The X and Y dimensions are 2400 Å.
- Fig. 2 Same as Fig. 1 except the ion fluence is $Q_2 = 10^{17}$ ions/cm².
- Fig. 3 Same as Fig. 1 except the ion fluence is $Q_3 = 10^{18}$ ions/cm².
- Fig. 4 Sputtered graphite surface topographs which show the dependence of surface morphology on sample temperature. The ion fluence and flux were fixed at $Q_2 = 10^{17}$ ions/cm² and $J_2 = 3.5 \times 10^{14}$ ions/cm² sec, respectively. The sample temperatures during bombardment were: (a) $T = 300\text{K}$, (b) $T = 600\text{K}$ and (c) $T = 900\text{K}$.
- Fig. 5 Topographs of the graphite surface shown in Fig. 1a, the smoothest of the surfaces sputtered at room temperature, collected at progressively higher magnifications. The image sizes are: (a) 1000 Å x 1000 Å, (b) 250 Å x 250 Å and (c) 50 Å x 50 Å. The sample has been sputtered with fluence $Q_1 = 10^{16}$ ions/cm² and flux $J_1 = 6.9 \times 10^{13}$ ions/cm² sec.
- Fig. 6 Topographs of the graphite surface shown in Fig. 2c, a sputtered surface with large short range roughness, collected at the same magnifications as in Fig. 5. The sample has been sputtered with fluence $Q_2 = 10^{17}$ ions/cm² and flux $J_3 = 6.9 \times 10^{14}$ ions/cm² sec.
- Fig. 7 Topographs of the graphite surface shown in Fig. 3b, a sputtered surface with large long range roughness, collected at the same magnifications as in Fig. 5. The sample has been sputtered with fluence $Q_3 = 10^{18}$ ions/cm² and flux $J_2 = 3.5 \times 10^{14}$ ions/cm² sec.

Fig. 8 Sawtooth shaped model surface profile which has corrugation $\sigma = 1$ at a lateral length scale of L . The apex angles of the regular features are 90° for these conditions and no serious artifacts caused by the convolution of tip shape into the image should occur for a typical probe tip scanning such a surface. This indicates that experimental topographs with $\sigma \leq 1$ should be free of tip related artifacts.

Fig. 9 (a) High magnification ($40 \text{ \AA} \times 40 \text{ \AA}$) STM image of unsputtered graphite. The familiar atomically resolved features are clearly seen.

(b) Random surface topograph artificially generated by feeding the signal from a white-noise generator into the STM data acquisition channel and collected at the same magnification as in (a).

Fig. 10 (a) Plot of the autocovariance functions $G(L)$ vs. L for the surfaces of Fig. 9a (solid line) and Fig. 9b (dotted line). Note the periodic signature in $G(L)$ for the periodic surface and the lack of correlation for all lengths except $L = 0$ for the random surface.

(b) Plot of the height correlation functions $\langle |h(\mathbf{q})|^2 \rangle_t$ vs. q calculated from the topographs shown in Fig. 9a (solid circles) and Fig. 9b (open circles). The correlation function calculated for the periodic surface of Fig. 9a contains peaks which correspond to the atomically resolved features seen in the STM topograph. On the other hand, the approximately constant value of $\langle |h(\mathbf{q})|^2 \rangle_t$ for the random surface indicates features of roughly equal height at all wavevectors.

Fig. 11 Plots of the corrugation σ vs. lateral length calculated from:

(a) the $2400 \text{ \AA} \times 2400 \text{ \AA}$ topographs of sputtered graphite shown in Fig. 1a (large dashes), Fig. 2c (solid line) and Fig. 3b (small dashes).

- (b) the high magnification ($50 \text{ \AA} \times 50 \text{ \AA}$) topographs of the same three surfaces as in (a), which are shown in Fig. 5c (large dashes), Fig. 6c (solid line) and Fig. 7c (small dashes).

These surfaces represent the extreme limits of roughness in the data set. Note that $\sigma < 1$ for all length scales, indicating the absence of tip related artifacts.

Fig. 12 Plots of autocovariance functions that show the changes in the behavior of $G(L)$ vs. L for increasing flux J (a, b and c: calculated from topographs in Figs. 1a, 1b and 1c, respectively) and for increasing fluence Q (a, d and e: calculated from topographs in Figs. 1a, 2a and 3a, respectively). The initial regions have been approximated as Gaussian in shape to permit the extraction of the auto-covariance length λ and the interface width δ .

Fig. 13 Temperature dependence of the autocovariance function, with ion fluence and flux fixed at $Q_2 = 10^{17} \text{ ions/cm}^2$ and $J_2 = 3.5 \times 10^{14} \text{ ions/cm}^2 \text{ sec}$, respectively. $G(L)$ is calculated from the topograph in: (a) Fig. 4a, $T = 300\text{K}$, (b) Fig. 4b, $T = 600\text{K}$, (c) Fig. 4c, $T = 900\text{K}$. Note the decrease in the interface width $\delta = \sqrt{G(0)}$. The autocovariance length λ decreases significantly only at the highest temperature, $T = 900\text{K}$.

Fig. 14 Plots of height correlation function vs. wavevector q showing the dependence on flux J of the correlation function $\langle |h(q)|^2 \rangle$, the interface width W and the correlation length ξ for the two fluences (a) $Q_1 = 10^{16} \text{ ions/cm}^2$ and (b) $Q_2 = 10^{17} \text{ ions/cm}^2$. The curves corresponding to the three fluxes are: $J_1 = 6.9 \times 10^{13} \text{ ions/cm}^2 \text{ sec}$ (filled circles), $J_2 = 3.5 \times 10^{14} \text{ ions/cm}^2 \text{ sec}$ (open squares) and $J_3 = 6.9 \times 10^{14} \text{ ions/cm}^2 \text{ sec}$ (filled triangles). The values of the crossover wavevector, $q_0 = 2\pi/\xi$, are

indicated in each curve and a $1/q^{2.7}$ dependence for large q is shown for comparison in (a). The error bars represent plus and minus one standard deviation.

Fig. 15 Dependence of the correlation function $\langle |h(q)|^2 \rangle$, the interface width W and the correlation length ξ on fluence Q for the two fluxes (a) $J_1 = 6.9 \times 10^{13}$ ions/cm² sec and (b) $J_2 = 3.5 \times 10^{14}$ ions/cm² sec. The curves corresponding to the three fluences are: $Q_1 = 10^{16}$ ions/cm² (open circles), $Q_2 = 10^{17}$ ions/cm² (filled squares) and $Q_3 = 10^{18}$ ions/cm² (open diamonds). The error bars have the same meaning as those in

Fig. 16 Dependence of the correlation function $\langle |h(q)|^2 \rangle$ on sample temperature T during bombardment: $T = 300K$ (open squares), $T = 600K$ (filled circles) and $T = 900K$ (filled diamonds). A $1/q^4$ dependence is shown at large q for comparison. The smoothing of the surfaces sputtered at higher temperatures is indicated by the overall decrease in the values of $\langle |h(q)|^2 \rangle$. Note the q^{-4} tail at large q for sputtering at $T = 900K$.

Fig. 17 Plots of height correlation functions showing the consistency of the scaling behavior of $\langle |h(q)|^2 \rangle$ over approximately four decades in wavevector q . The correlation functions were calculated from topographs of sizes $2400 \text{ \AA} \times 2400 \text{ \AA}$ (filled triangles), $1000 \text{ \AA} \times 1000 \text{ \AA}$ (open squares), $250 \text{ \AA} \times 250 \text{ \AA}$ (filled diamonds) and $50 \text{ \AA} \times 50 \text{ \AA}$ (open circles).

(a) $\langle |h(q)|^2 \rangle$ calculated from topographs of Figs. 1a, 5a, 5b and 5c for sputtering conditions $Q_1 = 10^{16}$ ions/cm² and $J_1 = 6.9 \times 10^{13}$ ions/cm² sec.

(b) $\langle |h(q)|^2 \rangle$ calculated from topographs of Figs. 2c, 6a, 6b and 6c for sputtering conditions $Q_2 = 10^{17}$ ions/cm² and $J_3 = 6.9 \times 10^{14}$ ions/cm² sec.

(c) $\langle |h(q)|^2 \rangle$ calculated from topographs of Figs. 3b, 7a, 7b and 7c for sputtering conditions $Q_3 = 10^{18}$ ions/cm² and $J_2 = 3.5 \times 10^{14}$ ions/cm² sec.

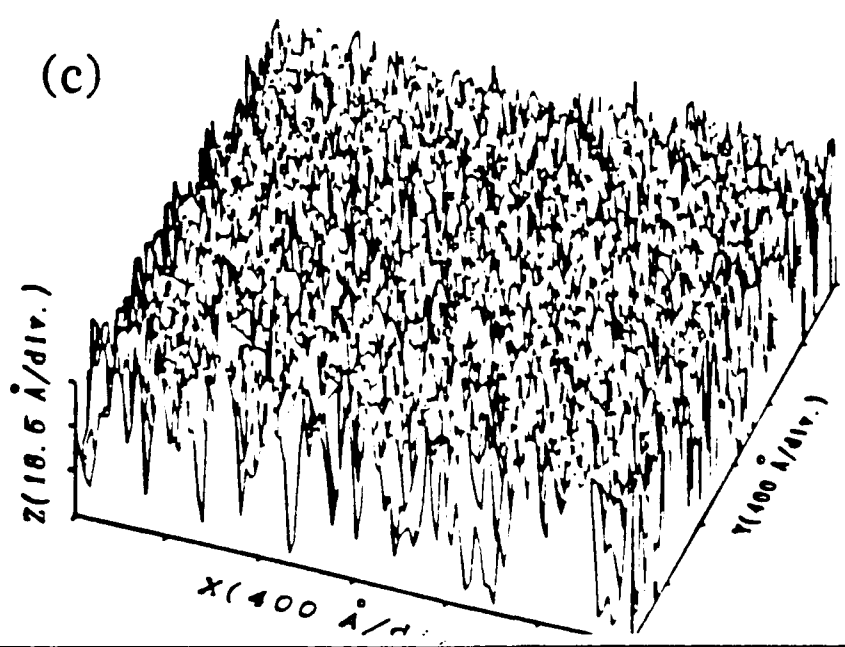
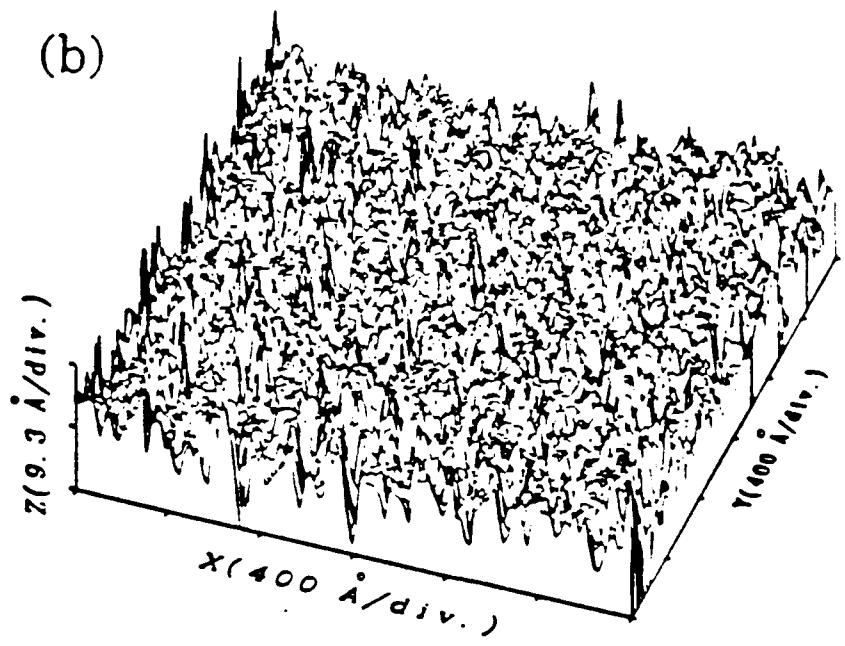
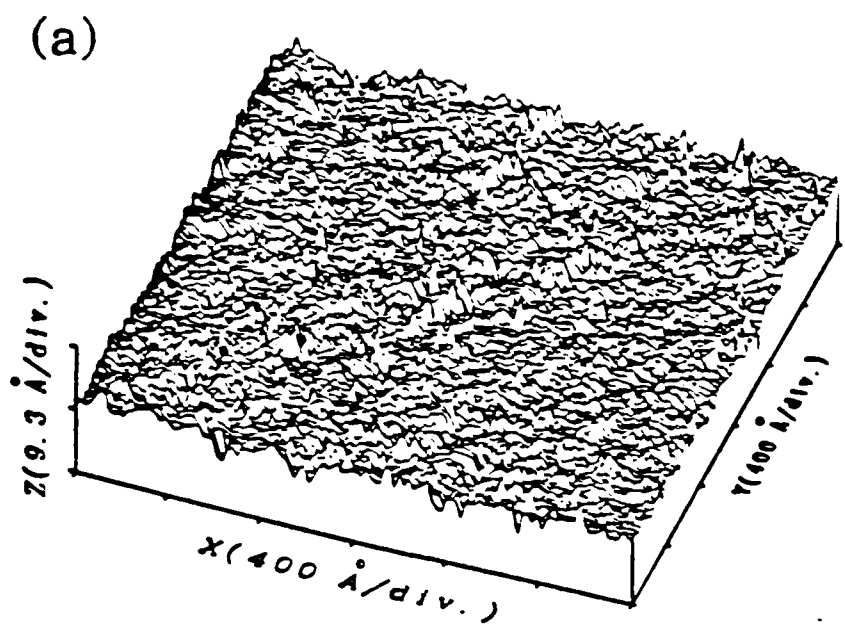
The curves do not overlap exactly because of small vertical shifts in $\langle |h(q)|^2 \rangle$ produced by the leveling of the different sized topographs. Note the consistency of the slopes for each set of curves.

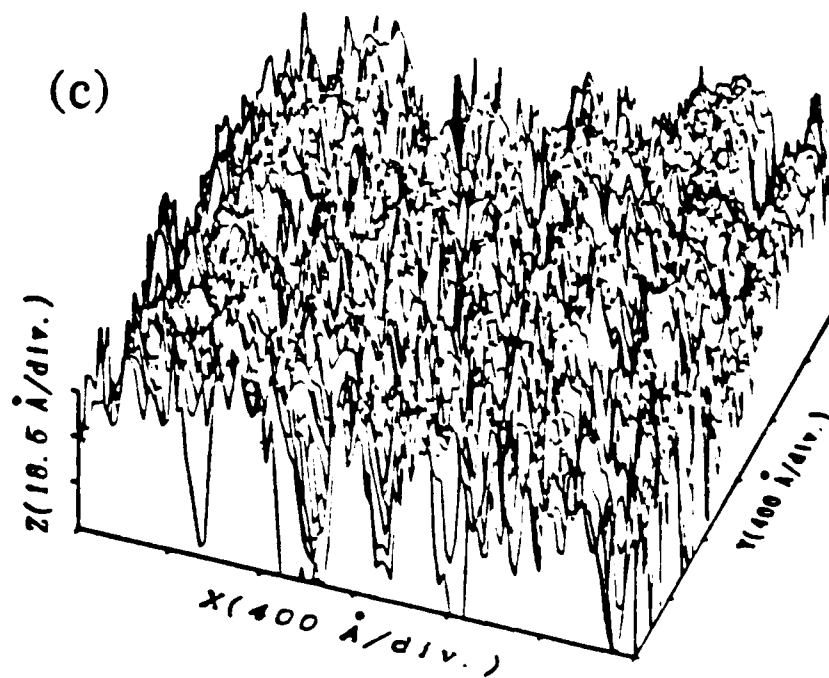
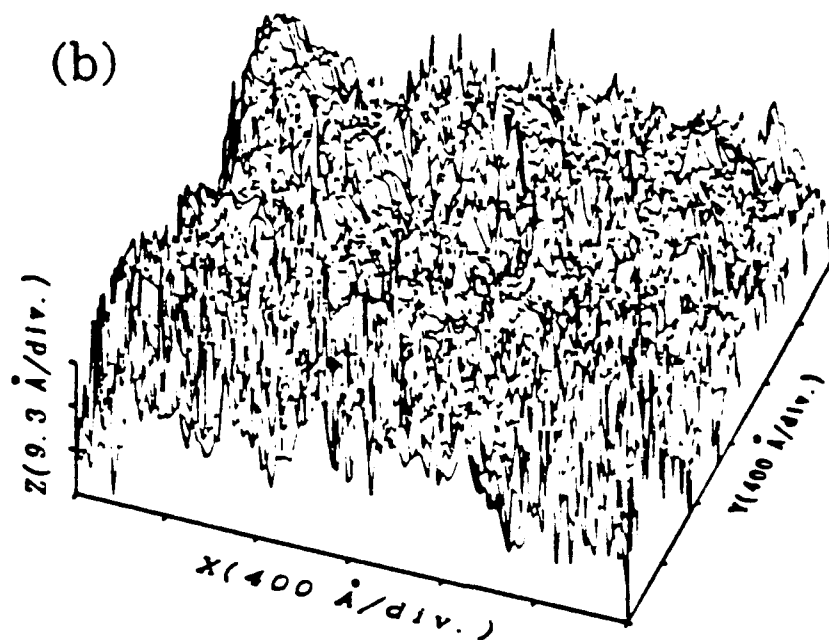
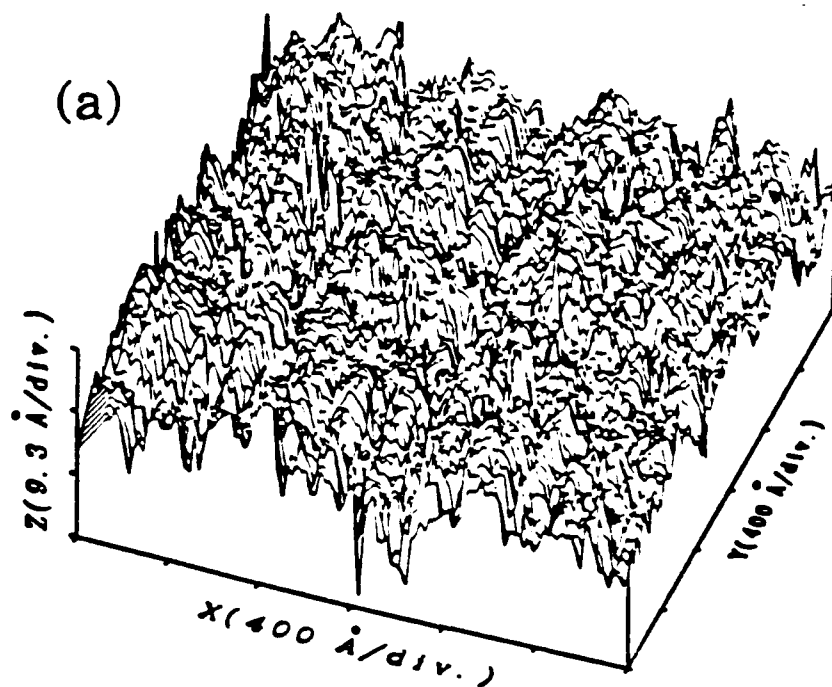
Fig. 18 Schematic diagram of the four smoothing mechanisms ^(surface diffusion, volume diffusion, sputter redeposition, and sputter removal) and their corresponding terms in Eqn. (5), the general continuum differential equation for the surface profile derived from linear response theory.

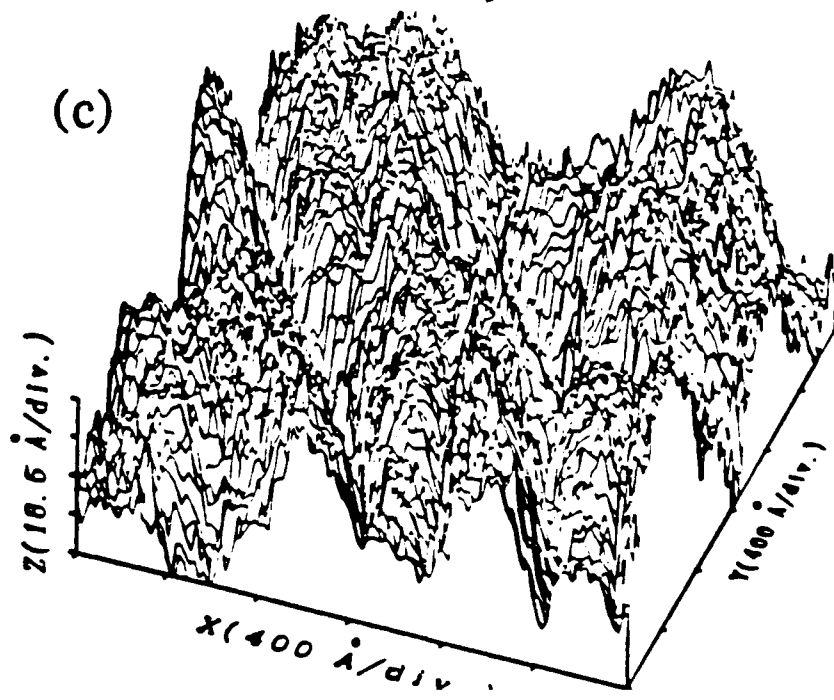
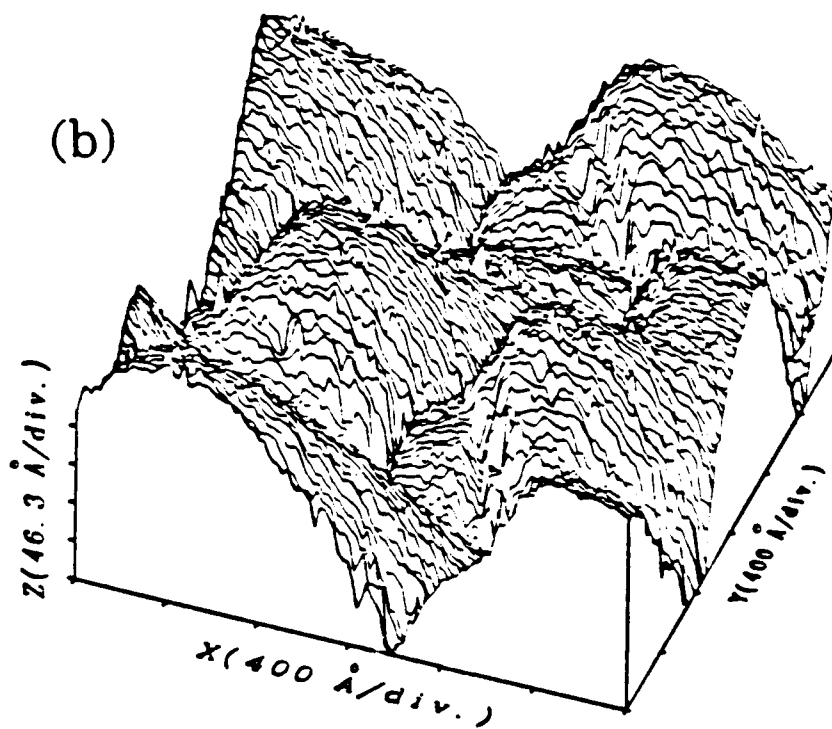
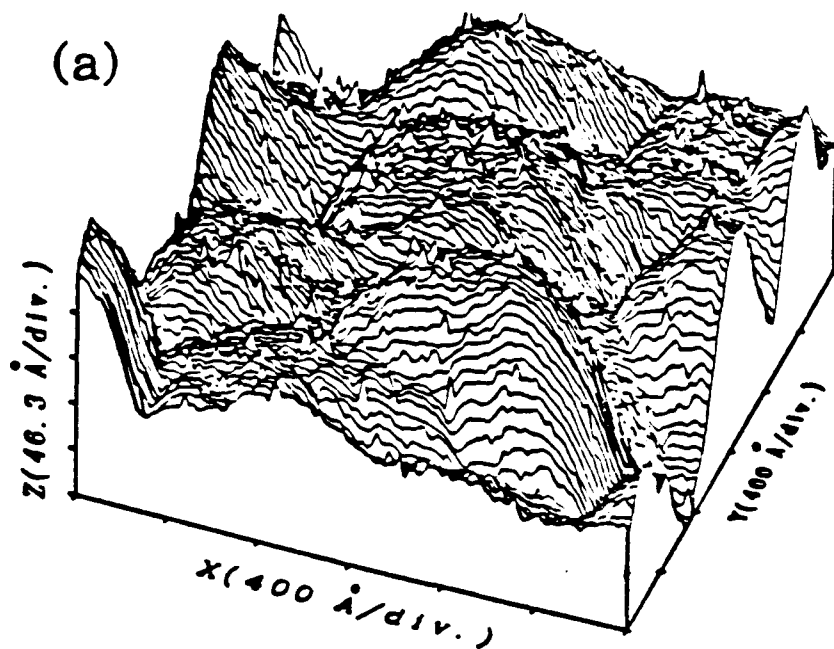
Table I. Summary of characteristic lengths (in Å) calculated from the STM topographs of Figs. 1 - 3. The autocovariance length λ and the interface width δ were determined from plots of the autocovariance function $G(L)$ vs. L . The correlation length ξ and the interface width W were determined from plots of the height correlation function $\langle |h(q)|^2 \rangle$ vs. q . In addition, the bottom row shows values for the interface width δ_{Poisson} calculated from an estimate of the surface roughening due solely to shot noise. For this estimate, the roughening follows the Poisson statistics of the random ion bombardment (and material removal) process.

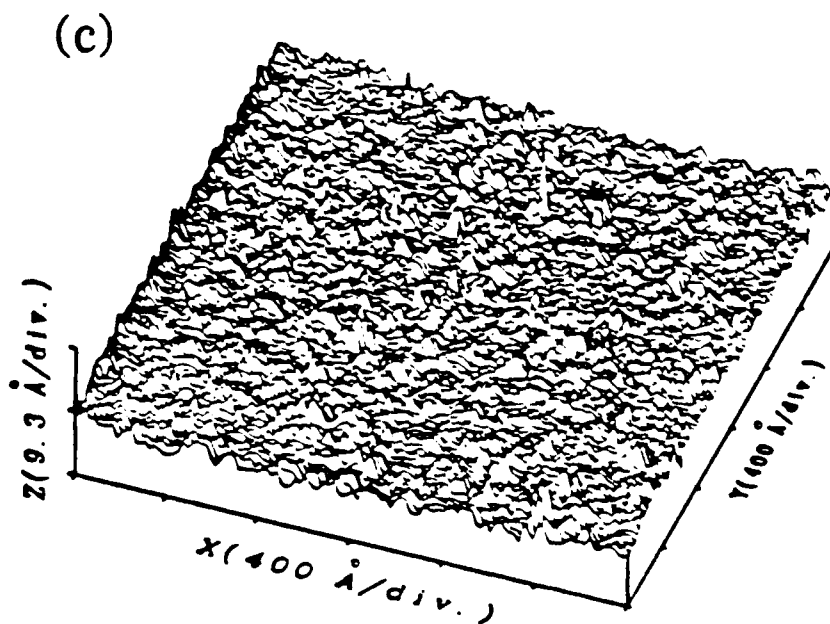
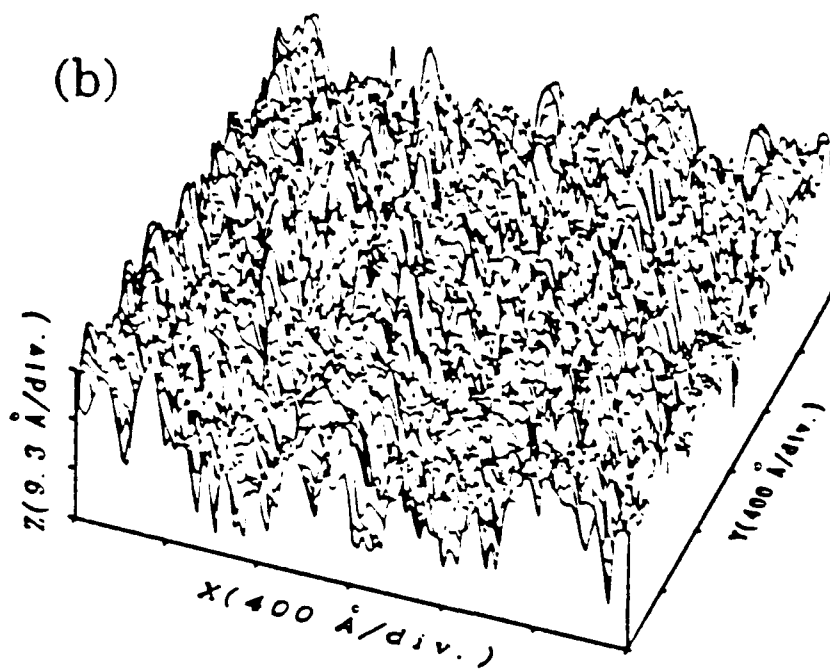
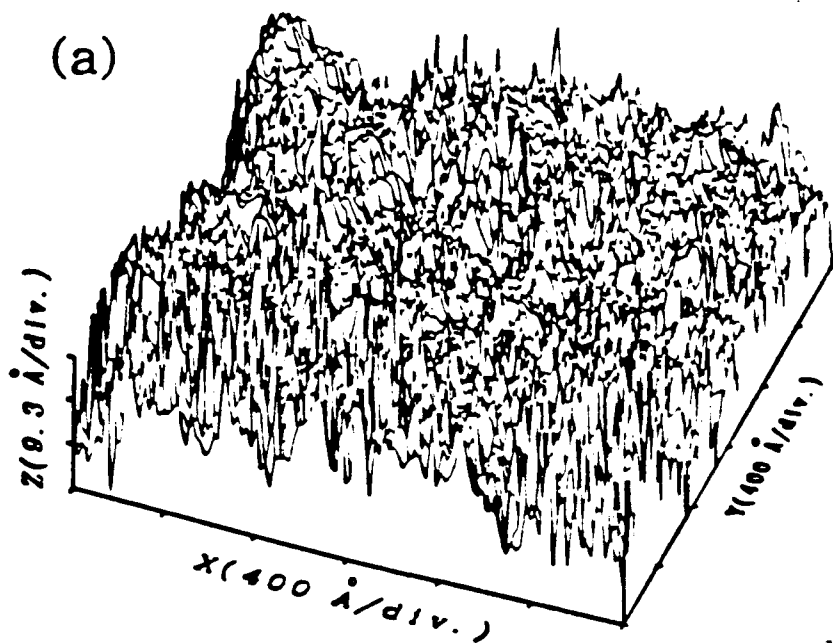
Table I. Summary of Characteristic Lengths (in Å) Calculated from STM Topographs

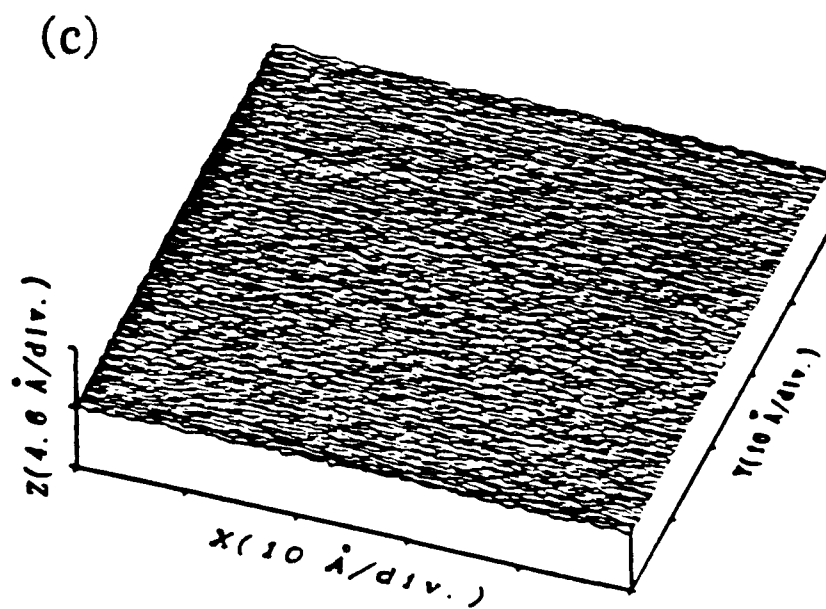
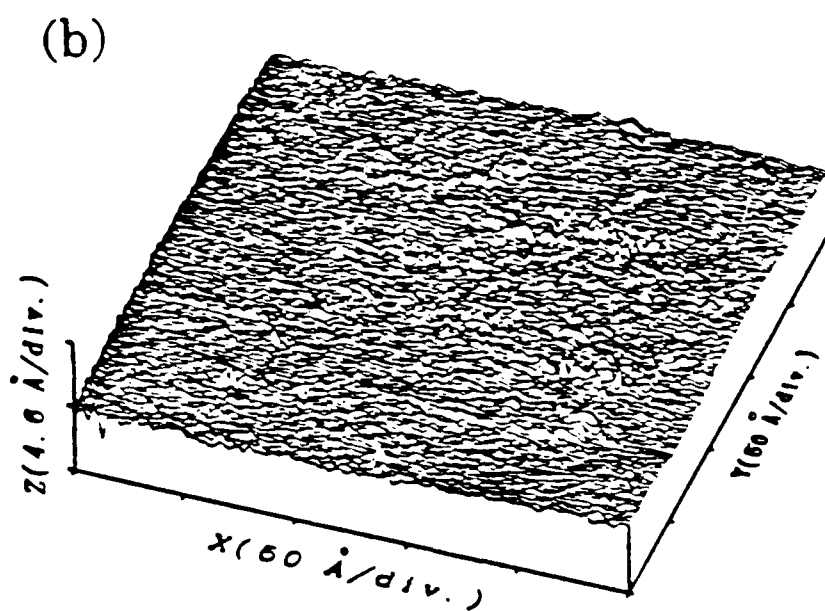
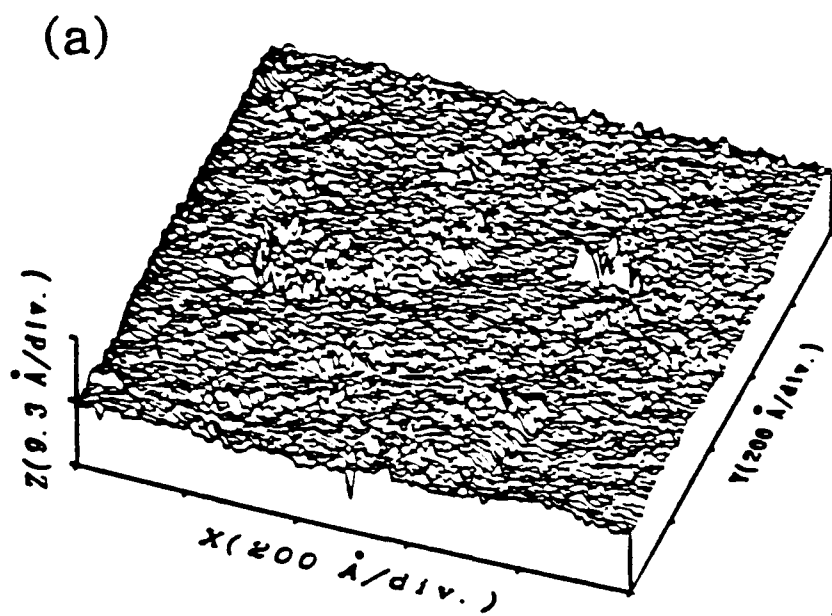
		Q_1	Q_2	Q_3
J_1	λ	33	135	235
	δ	1.0	3.9	43
	ξ	282	686	1200
	W	4.57×10^{-3}	4.33×10^{-2}	5.67×10^{-1}
J_2	λ	40	100	210
	δ	3.3	8.2	92
	ξ	267	533	1200
	W	8.23×10^{-3}	9.34×10^{-2}	2.69
J_3	λ	20	33	220
	δ	20.2	13.1	31.6
	ξ	185	480	960
	W	5.95×10^{-2}	2.03×10^{-1}	4.46×10^{-1}
δ_{Poisson}		6.7	21	67

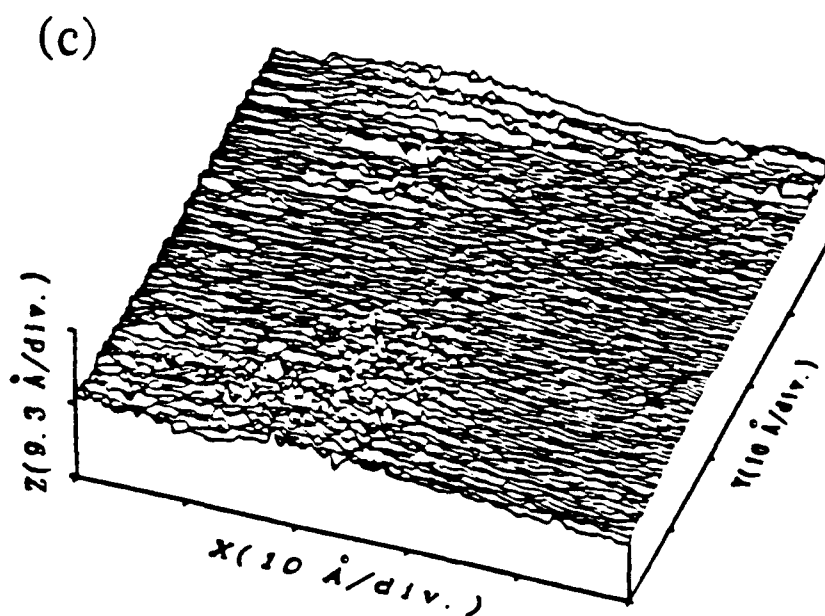
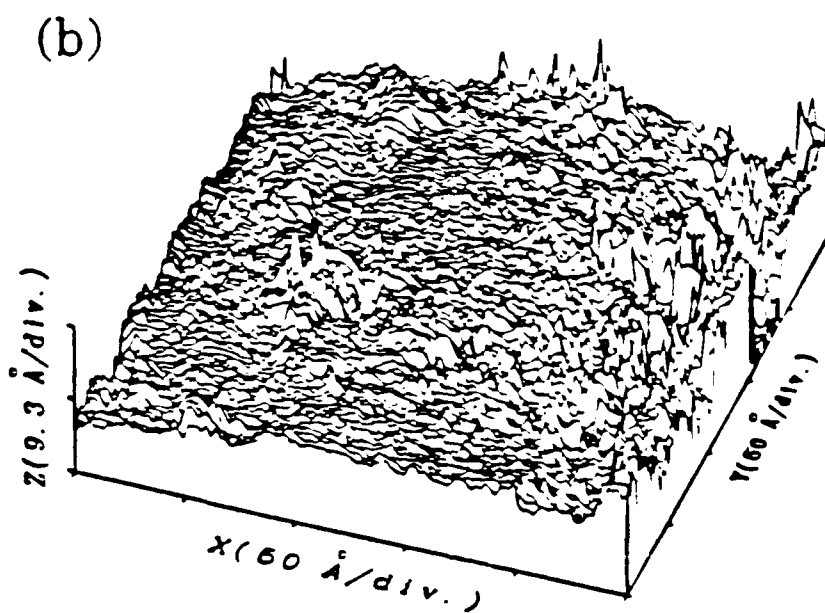
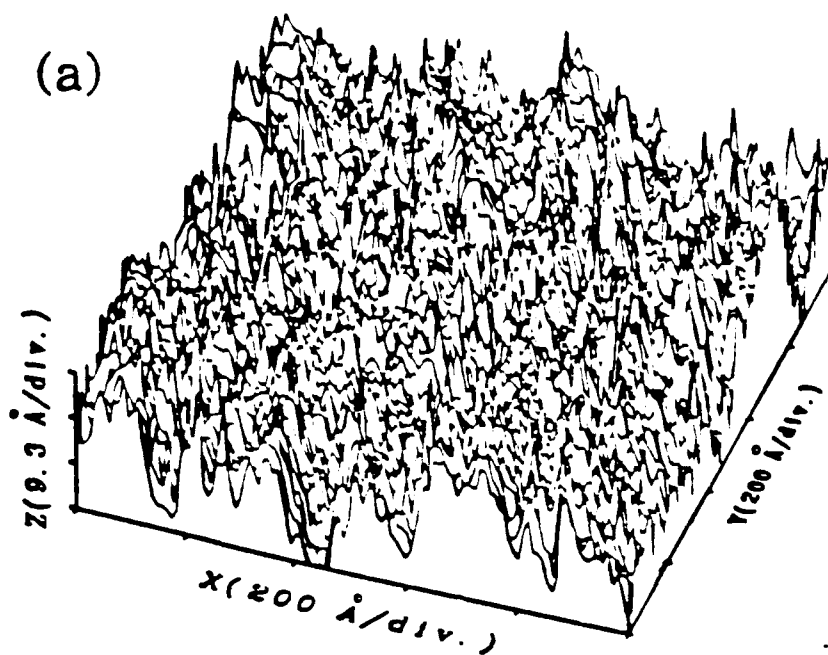


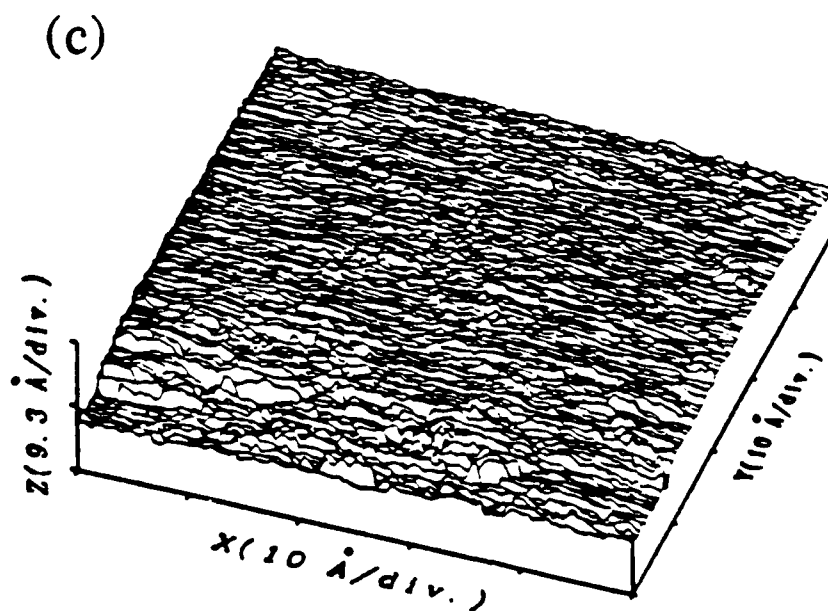
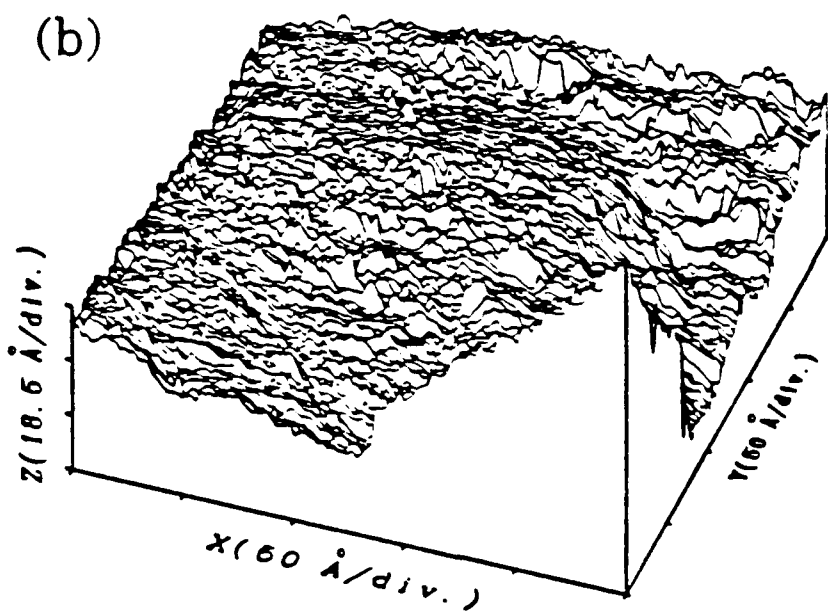
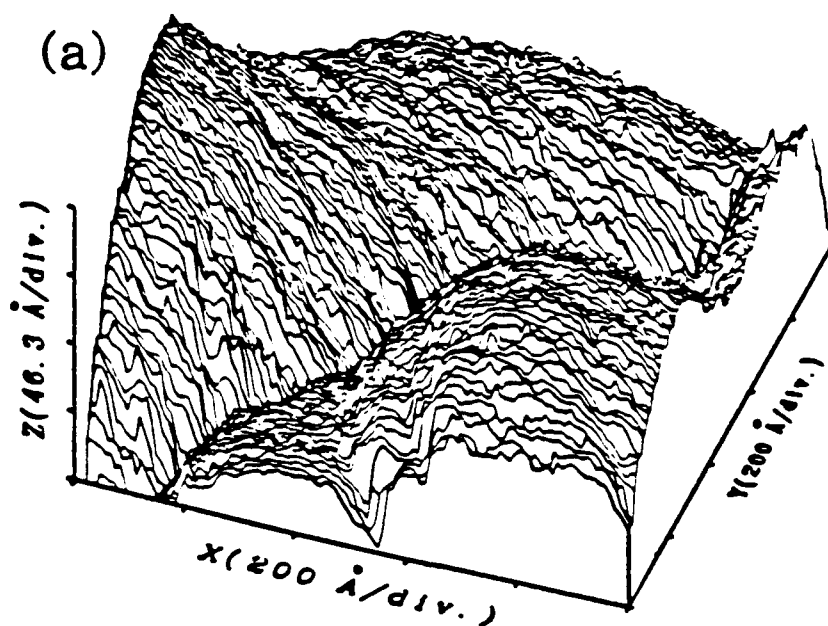


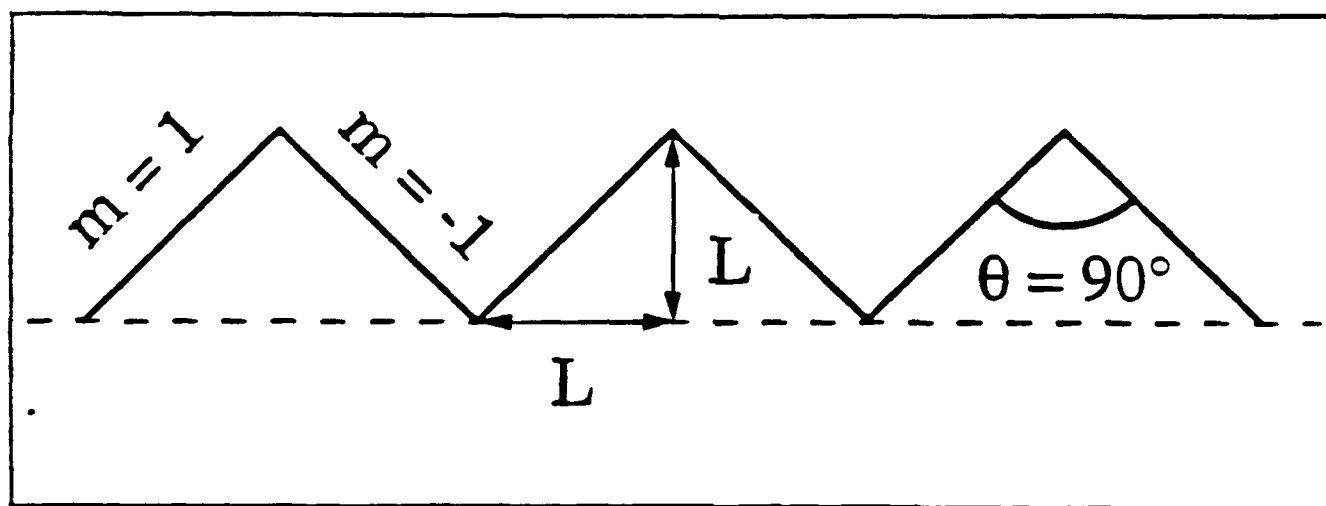












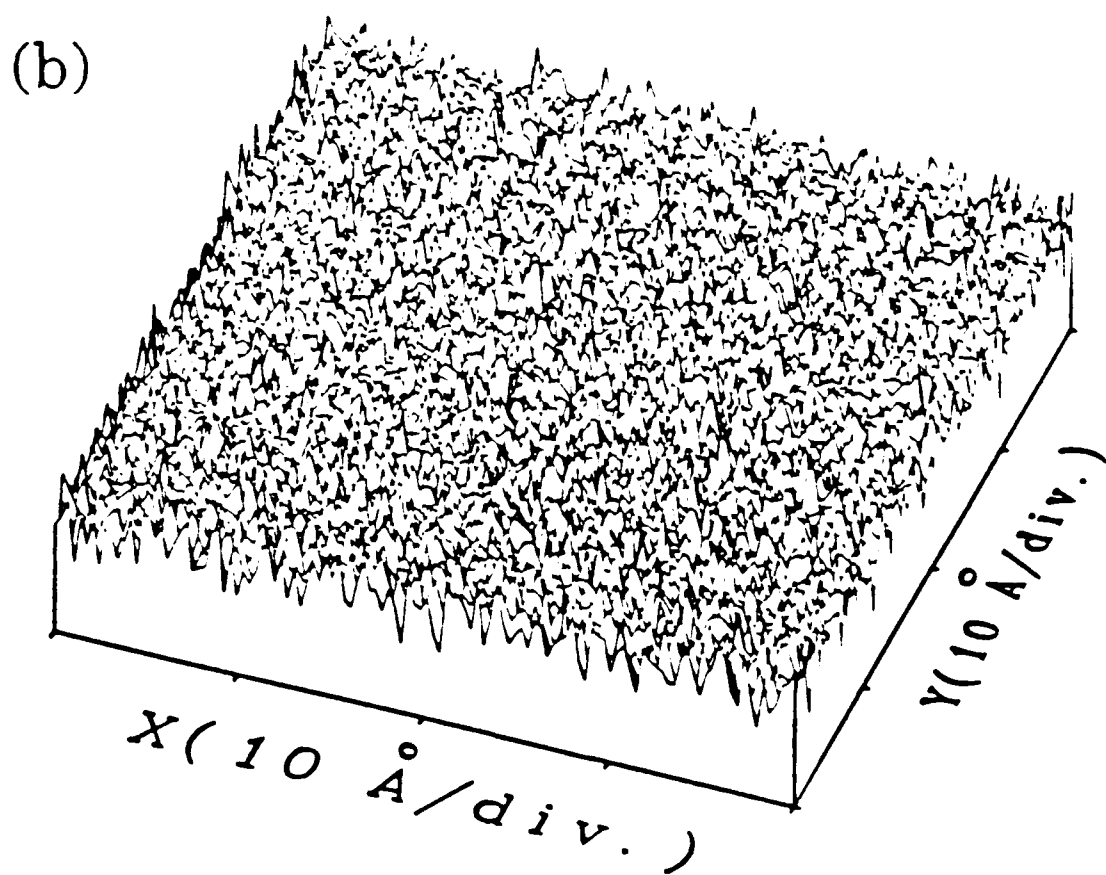
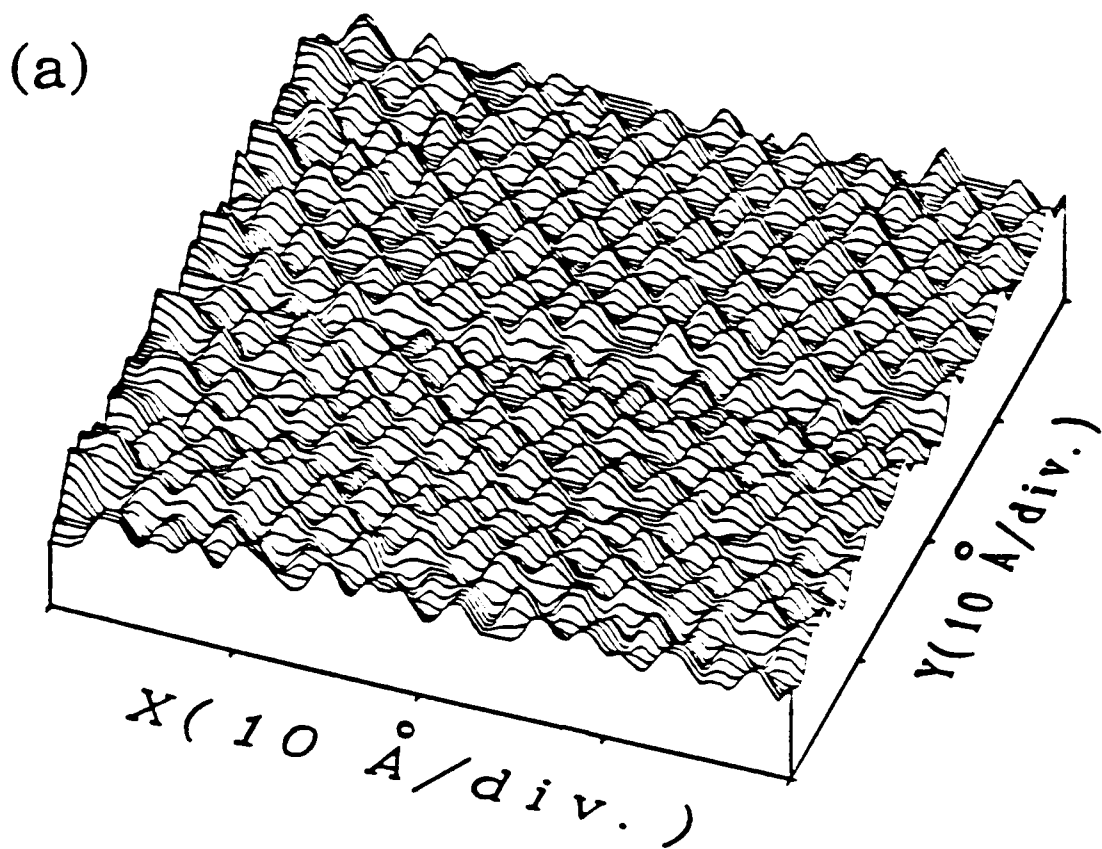


Fig. 10.

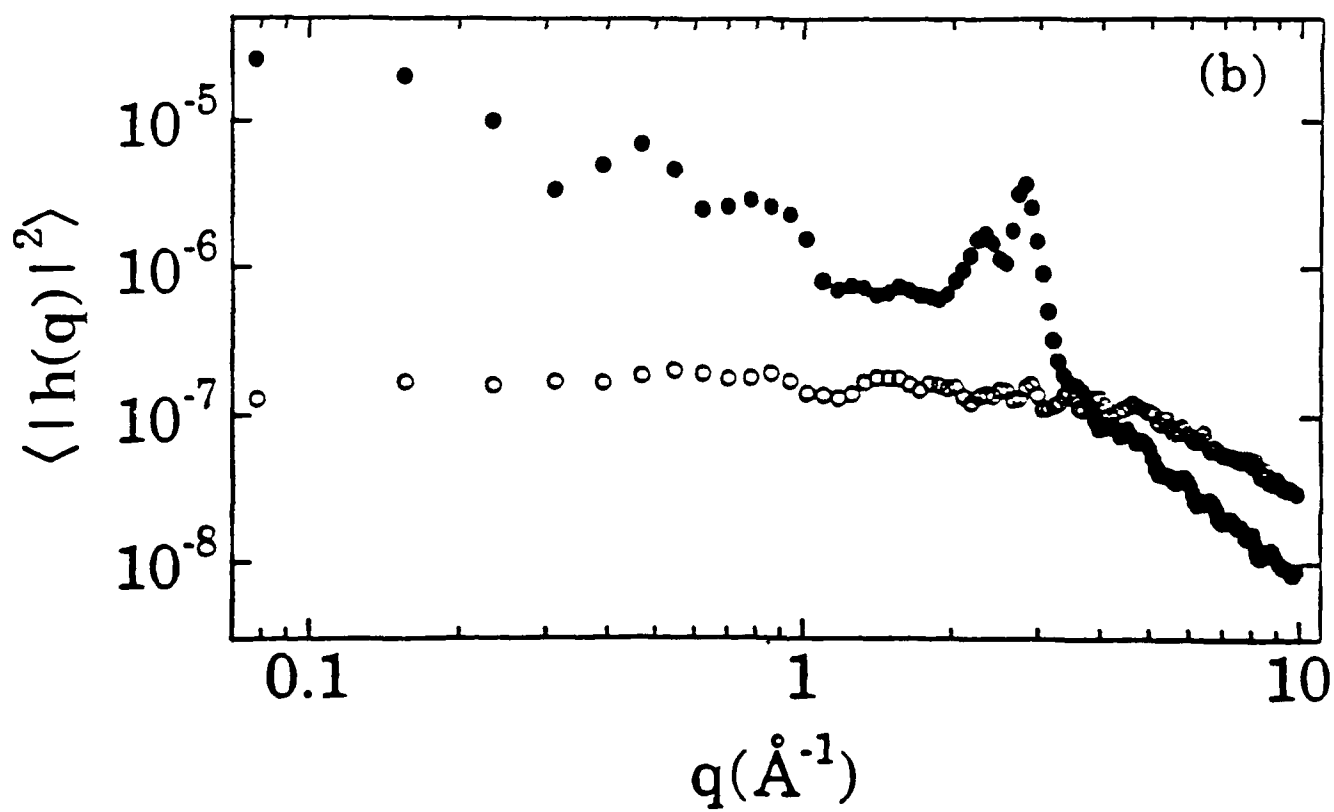
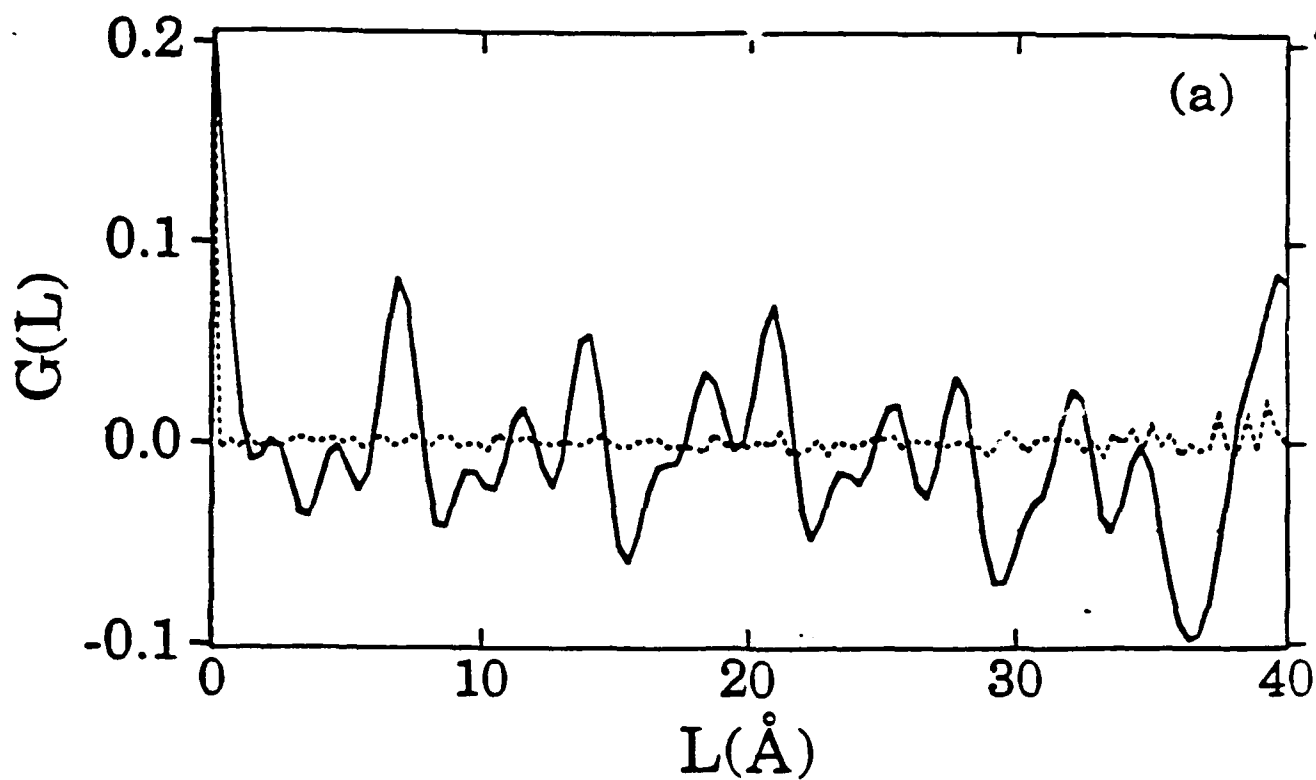
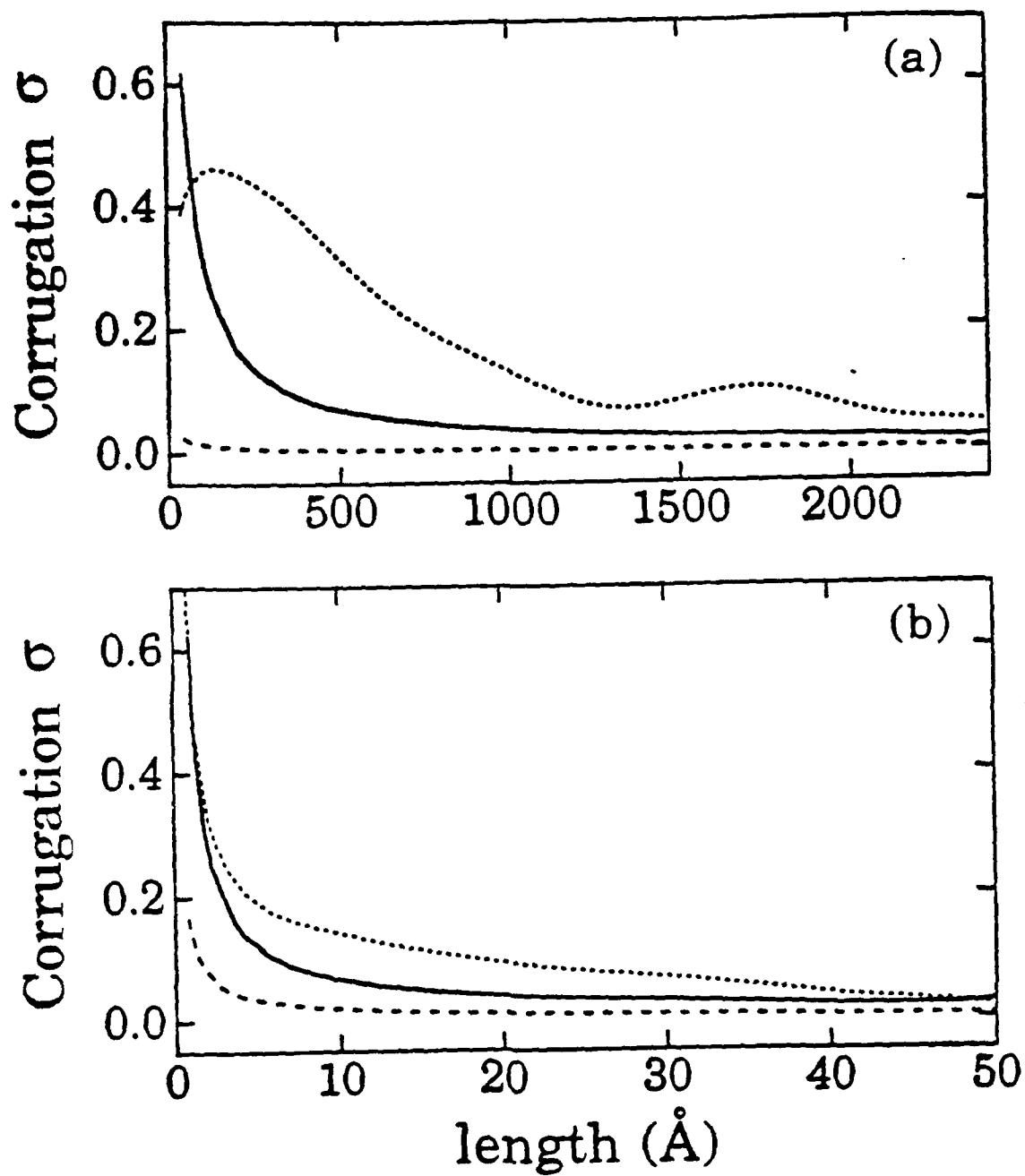
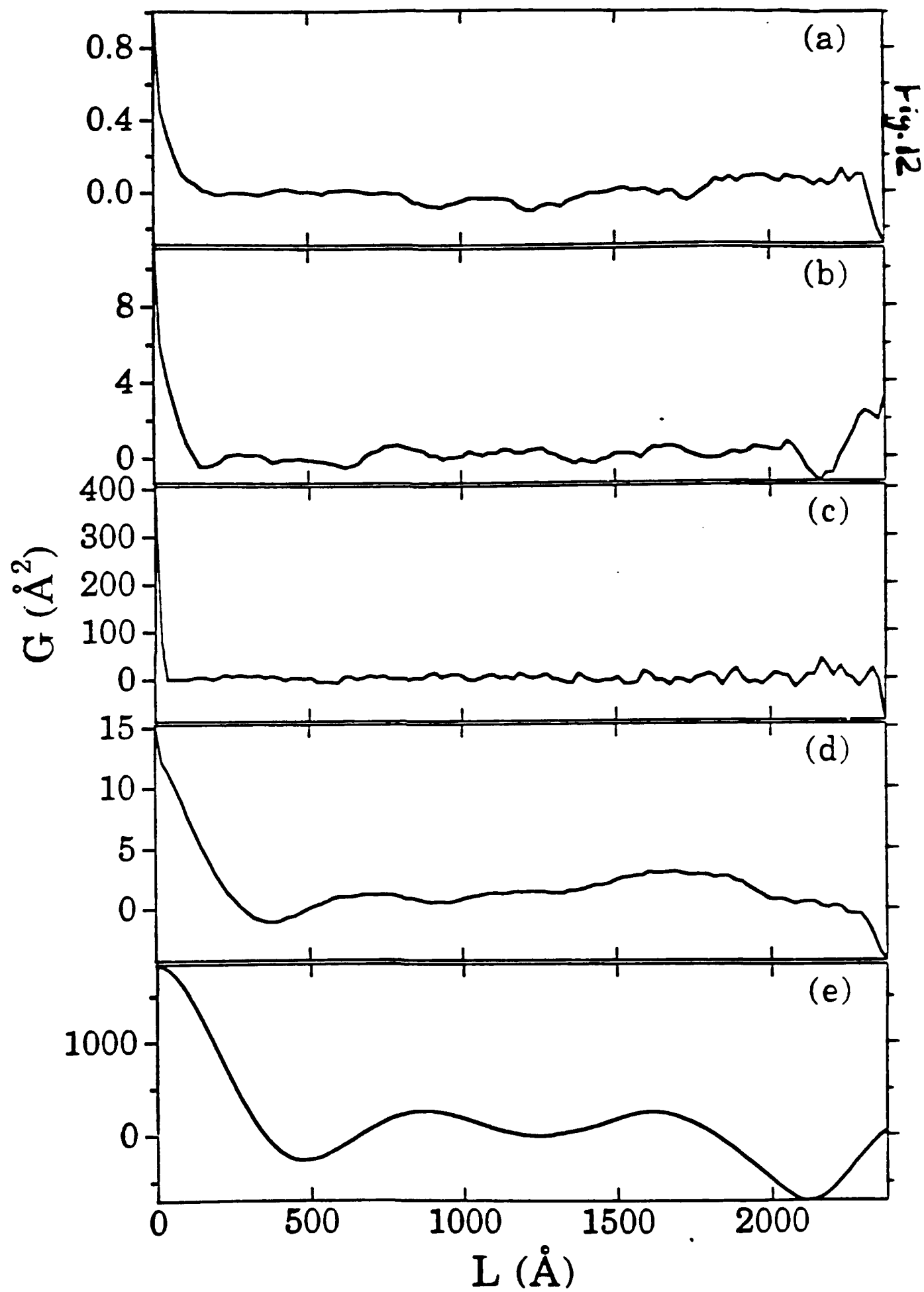


Fig. 11.





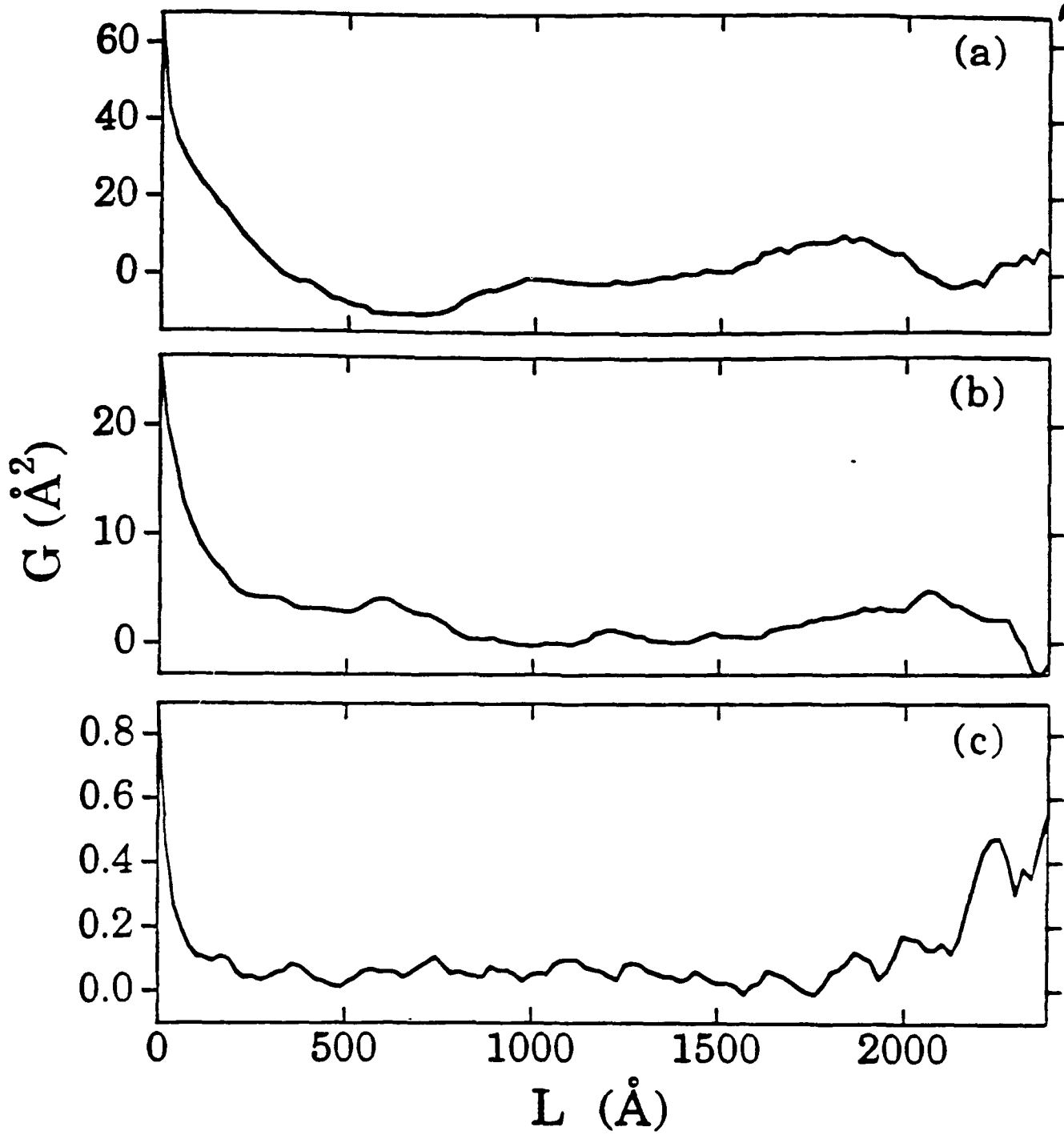


Fig 14

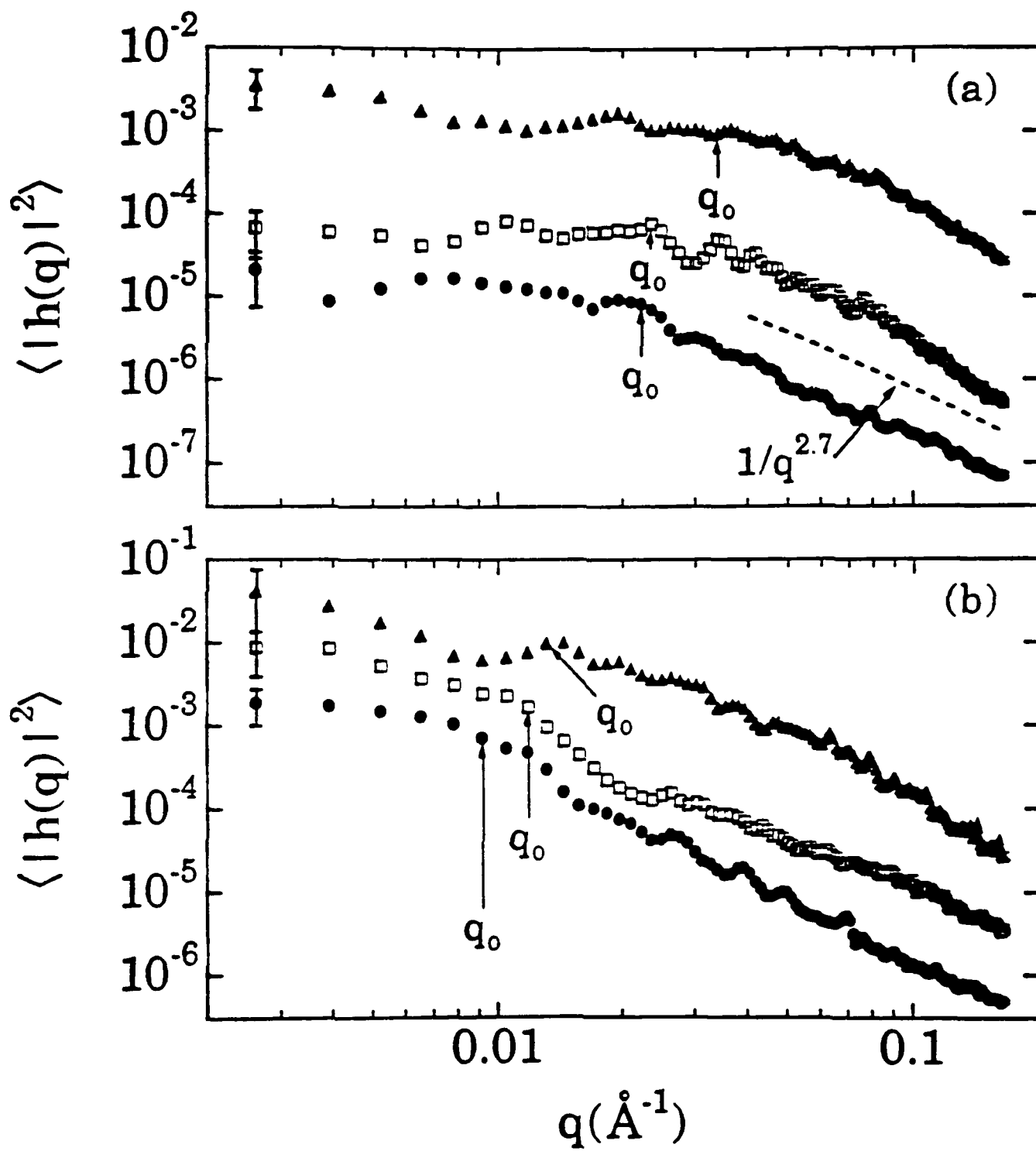
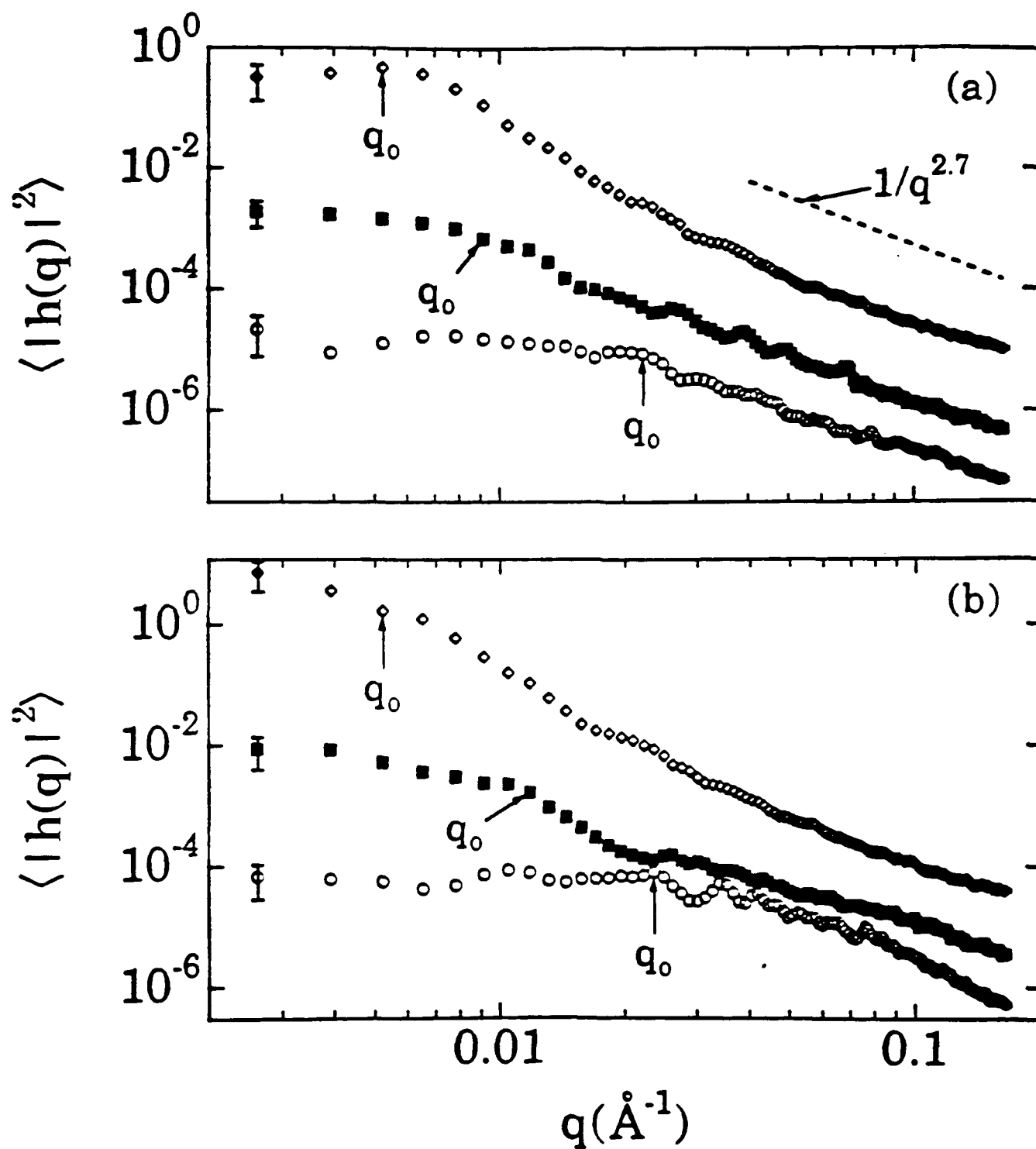


Fig 15.



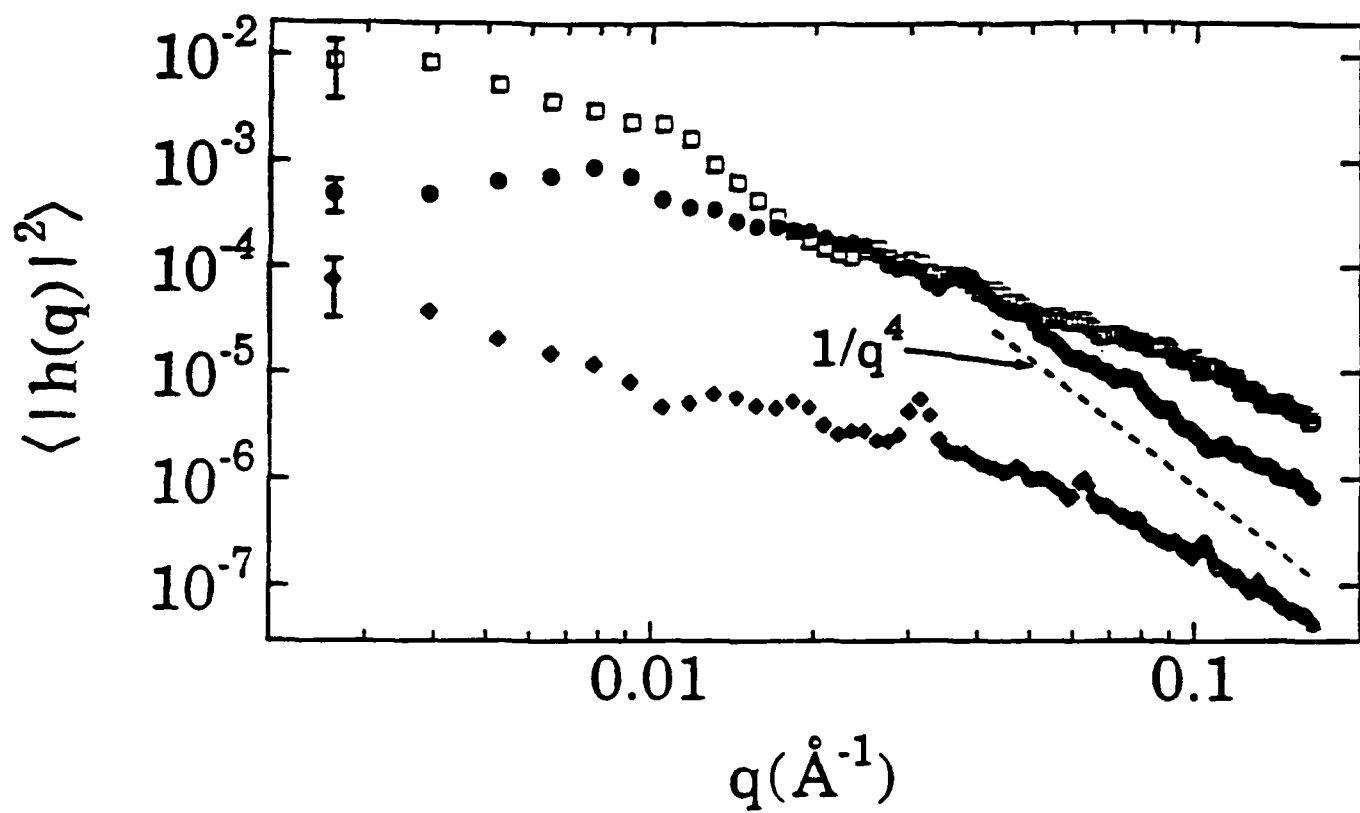


Fig.17

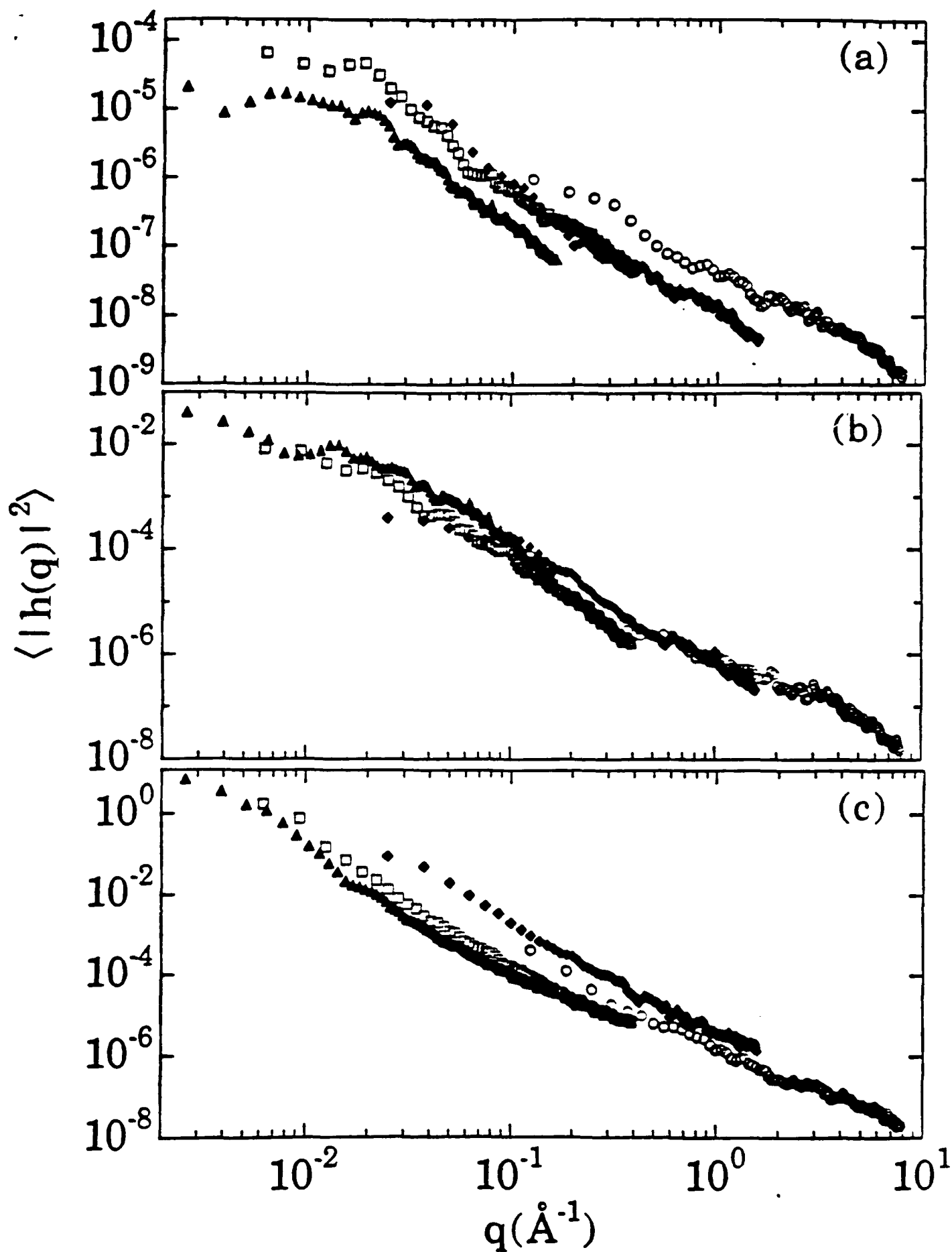


Fig. 18

